symmetry

Article

Swing-By Applications and Estimation of the Van Allen Belts' Radiation Exposure for a Spacecraft in a Low Thrust Transfer to the Moon

Rodrigo N. Schmitt [1,*], Antonio F. B. A. Prado [1,2], Alexander Sukhanov [3] and Vivian M. Gomes [4]

[1] National Institute for Space Research (INPE), Av. dos Astronautas—Campus do CTA, Sao Jose dos Campos 12227-010, SP, Brazil; antonio.prado@inpe.br
[2] Academy of Engineering, Peoples' Friendship University of Russia (RUDN University), 6 Miklukho-Maklaya Street, Moscow 117198, Russia
[3] Space Research Institute (IKI) of the Russian Academy of Sciences, Profsoyuznaya Street, 84/32, Moscow 117997, Russia; sukhanov@cosmos.ru
[4] São Paulo State University (UNESP), Av. Dr. Ariberto Pereira da Cunha, 333-Pedregulho, Guaratinguetá 12516-410, SP, Brazil; vivian.gomes@unesp.br
* Correspondence: rodrigo.schmitt@alumni.usp.br

Abstract: This paper presents a handful of the underlying properties of a spacecraft's transfer from a low Earth orbit (LEO) to the moon's orbit using an electric propulsion (low-thrust) system. The use of analytical and numerical-analytical modeling in complex natural and technical processes is a key factor in this issue of Symmetry, which has been thoroughly explored in this paper. First, an optimization problem was considered to find the locations and lengths of the thrust arcs that maximizes the final mass of the spacecraft for a number of transfer orbits, thereby limiting the scope of trajectories to the most fuel-efficient ones. In addition to this, the Van Allen belts were modelled according to the density of electrons and protons in each point of space, in order to measure the total radiation absorbed by the spacecraft through an integration of the density of particles over the corresponding time. The simulations were then able to predict the relationship between the fluence of the particles and several initial parameters, such as the initial orbit's eccentricity and the propulsion system's characteristics. Then, a multi-linear regression and an artificial neural network were fitted to the data through a regression that related the fluence of protons and electrons as a function of the following parameters: mission time, specific impulse, thrust, final mass (i.e., propellant consumption) and the initial height of the perigee, eccentricity and inclination. This analysis was proven to be powerful due to the expressive values from statistical tests, showing underlying positive correlations between thrust, mission time and final spacecraft mass with the fluence of particles, and negative correlations between specific impulse, initial orbit eccentricity, inclination and the height of the perigee with the fluence of particles. Finally, an analysis of a swing-by maneuver was also carried out, together with the radiation incidence, revealing hidden dependencies of the increments in energy and velocity with respect to the fuel consumption, radiation absorption, propulsion system and initial orbit parameters.

Keywords: astrodynamics; Van Allen belts; low thrust; swing-by; mission analysis

check for updates

Citation: Schmitt, R.N.; Prado, A.F.B.A.; Sukhanov, A.; Gomes, V.M. Swing-By Applications and Estimation of the Van Allen Belts' Radiation Exposure for a Spacecraft in a Low Thrust Transfer to the Moon. *Symmetry* **2022**, *14*, 617. https://doi.org/10.3390/sym14030617

Academic Editor: Jan Awrejcewicz

Received: 12 January 2022
Accepted: 1 March 2022
Published: 19 March 2022

1. Introduction

The context of the problem studied here is the transfer orbit of a spacecraft from a low Earth orbit (LEO) towards the moon using low-thrust systems. The moon was chosen as the target, given the return of public interest in lunar exploration missions, as well as the possibility of a swing-by maneuver that optimizes transfers to other planets. The specific impulse of a low-thrust propulsion system is five to ten times greater than those of ordinary chemical propulsion systems, which translates to higher efficiency. On the one hand, the thrust of this type of propulsion is very low: the acceleration induced is of the order of

10^{-4} to 10^{-5} m/s^2. On the other hand, the low thrust can permanently function for months, which leads to a spiral ascent transfer from LEO, with hundreds of revolutions around the Earth lasting for months. Thus, the spacecraft will cross the Van Allen belts hundreds of times during its ascent, what may pose a hazard to its electronic equipment due to the radiation exposure. The following optimization problem can then be considered: finding the locations and lengths of the thrust arcs that maximize the final spacecraft mass (i.e., minimize the propellant consumption) under the constraint on the radiation dose absorbed during the transfer.

Exploring the regularities of complex phenomena in mechanics and control has been made possible through the use of tools such as optimization theory. This special issue of Symmetry also aims at tackling complex problems both in natural and technical aspects, which was carried out both via analytical modeling of the Van Allen belts and other natural processes, such as a model of the Earth's magnetic field.

The dynamical system during the ascent is constituted by the spacecraft starting its motion in orbit around the Earth—after being detached from the rocket—in a parking orbit with given orbital elements. After that, the spacecraft is powered by low thrust until it reaches an orbital energy level of zero. The engine operates in an "on-off" mode, with thrust arcs near perigee and coast arcs in the rest of the orbit, as illustrated in Figure 1. A family of transfer orbits is built using the total transfer time as a parameter. This means that, based on its value, optimization techniques are used to determine the number and duration of the thrust arcs.

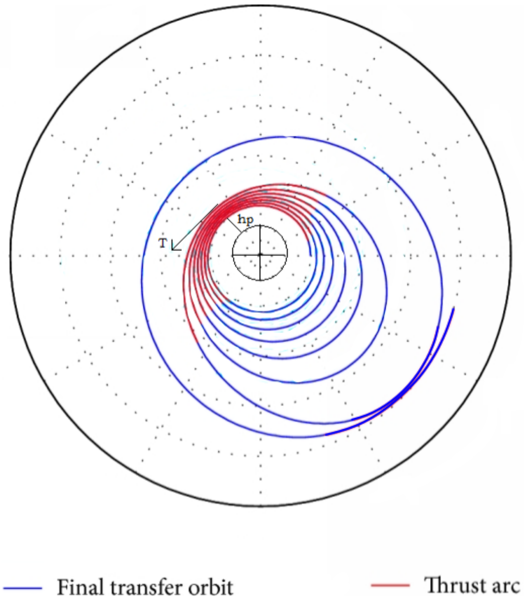

Figure 1. Trajectory of the spacecraft escaping from the Earth [1].

During the transfer, the total time that the spacecraft spends inside the radiation belts is calculated by dividing the belts in several regions and integrating the flux in time in each of them, as well as the respective proton and electron integral omnidirectional fluxes accumulated by the spacecraft inside that region. The omnidirectional flux is defined by particles coming from all directions with an energy greater than the threshold energy chosen. It is then possible to determine the propellant consumed, the total transfer time, the time the spacecraft spends inside the belts and the total radiation it absorbs during the transfer. This information is sufficient to build plots that show the options available for a mission designer. Additionally, in order to explore regular trends between the parameters involved in these low thrust trajectories, regressive models were created on top of these plots using both least-squares Linear Regression and Artificial Neural Networks (ANN).

2. Materials and Methods

2.1. The Optimization Method

Most of the existing electric propulsion systems are close to the constant exhaust velocity (CEV) design, for which the jet stream has a constant speed and the mass flow rate is limited; i.e., the value $\dot{m}_P$, where m_P is consumed propellant mass, limited by a constant value γ: $0 \leq \dot{m}_P \leq \gamma$. This is why the CEV low-thrust model is considered in this paper. Since the thrust is very low, the spacecraft ascent in the Earth's sphere of influence (SOI) occurs in a spiral trajectory with a large number of revolutions. The problem is to optimize the low thrust, i.e., to find a control method for the thrust as a function of time, solving one of the following tasks:

- The achievement of a specified transfer target for a given time with a minimum propellant consumption and hence the maximum final mass of the spacecraft;
- Minimizing the transfer time with a given amount of propellant;
- Maximizing the spacecraft's orbital energy for a given transfer time with a given amount of propellant.

The first of these tasks is considered and slightly generalizedin this paper: to find a control method of the thrust, providing the maximum spacecraft mass versus the transfer time for a given transfer target.

According to optimization theory [2], the optimal control of the CEV thrust is defined by the so-called switching function $\kappa = \kappa(t)$ in the following way:

- if $\kappa > 0$ then $\dot{m}_P = \gamma$ (maximum thrust);
- if $\kappa < 0$ then $\dot{m}_P = 0$ (zero thrust);
- if $\kappa = 0$ then $0 \leq \dot{m}_P \leq \gamma$ (intermediate thrust).

This rule is illustrated in Figure 2.

In fact, the intermediate thrust is never used in practice. Thus, the optimal CEV transfer trajectory consists of thrust arcs with maximal thrust ($\dot{m}_P = \gamma$) and coast arcs with no thrust ($\dot{m}_P = 0$). As is well known, if the thrust is impulsive, the optimal impulses are located in the perigee for the ascent in the Earth's—or other planet's—SOI. So, in the case of electric propulsion, the thrust arcs are located at the perigee of each trajectory. The problem is to determine the optimal positions of the thrust arcs with respect to the perigee and their optimal lengths. For non-circular orbits, the further the thrust application is from the perigee, the less effective is the thrust, compared to the application at perigee. Due to this fact, if ΔV_i and ΔV are the characteristic velocities necessary for the transfer between two given orbits by means of impulsive and low thrust, respectively, then $\Delta V > \Delta V_i$. The value $\delta V = \Delta V - \Delta V_i$ is the so-called gravity loss.

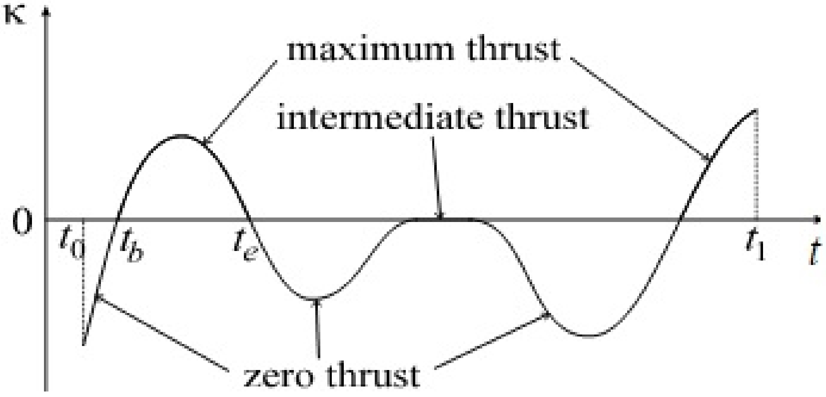

Figure 2. Switching function and thrust control versus transfer time.

The problem is now reduced to the minimization of the total gravity loss δV during the transfer and, thus, the maximization of the final spacecraft mass. The thrust arcs are assumed to be symmetric with respect to the perigee. Let E be the eccentric anomaly of the endpoint of the thrust arc; then the thrust arc is located between $-E$ and E. It is clear from what is written above that, for a given E, the gravity loss at each revolution depends on the revolution eccentricity e: a larger e should have smaller values for E. Now it is sufficient to find the dependence of E on e by providing optimal thrust lengths for all revolutions. This is a complicated problem; this is why it has been suggested to use the following empirical expression [3–5]:

$$E = F(1 - ce^{p}) \tag{1}$$

where F is an angular parameter, varying between 10° and 180° (corresponding to the longest and shortest transfer time, respectively); e is the eccentricity of the orbit being analyzed; and c and p are parameters varied within the limits $-1 < c < 1$ and $0 < p < 2$. The values of the parameters corresponding to the maximal final spacecraft mass for a given transfer time are selected. Varying the parameters F, c and p within the given limits, the values of the parameters giving the minimum propellant consumption (and hence the maximum spacecraft final mass) may be found for each transfer time.

Equation (1) was derived based on the analysis of the optimal thrust arcs. An analysis of thousands of transfer trajectories with various initial data has shown that the final spacecraft mass is very close to the one corresponding to the optimal thrust arcs.

2.2. Earth's Magnetic Field Model

Earth's geomagnetic field B consists of three distinct components: the nuclear field, the crust field and the external field. The nuclear field comes from the convective movement of conductive fluids from the terrestrial nucleus, whereas the crust field comes from superficial anomalies associated with ferromagnetic materials from the Earth's crust, which undergoes geological and tectonic movements. The nuclear and crust fields make up more than 99% of field B in LEO. However, the external field B_e is derived mainly from extraterrestrial sources, such as the solar wind, which varies quickly with the solar cycle of about 11 years and is intrinsically related to the geomagnetic activity and solar interactions. Models of the external components do exist, but are of limited importance to our models of the Van Allen belts [6].

The internal geomagnetic field can be modeled roughly by a magnetic dipole inclined in -11 degrees with respect to the geographic North, with magnitude $M = 8 \times 10^{25}$ G·cm^2. The field generated by M in spherical coordinates (R, θ, ϕ) is given by:

$$B_i = -\frac{M}{R^2}\sqrt{3cos\theta + 1} \tag{2}$$

This approximation is refined using the expansion of the scalar magnetic potential in spherical harmonics. B_i thus has a maximum of 0.6 G in the polar region and a minimum of 0.3 G near the magnetic equator [7].

A charged particle undergoes the influence of this magnetic field and will follow a helical trajectory around the field line, also known as a cyclotron, as illustrated in Figure 3.

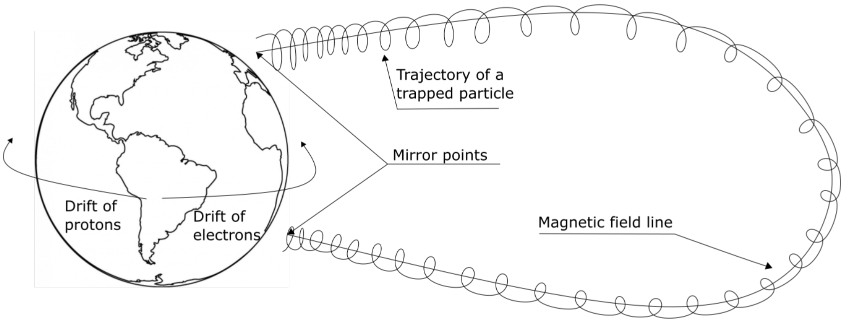

Figure 3. Movement of charged particles due to the interaction with the Earth's magnetic field [8].

By conserving a few physical parameters, such as the linear momentum of the particle, it is possible to use two variables to describe the geomagnetic field: the system B-L, in which a population of particles is described in terms of the flux of particles as a function of the values of B and L. The dimensionless quantity L is defined by:

$$L = \frac{R_0}{R_e} \tag{3}$$

where R_0 is the radial distance in which the field line crosses the magnetic equator, and R_e is the Earth's equatorial radius, 6378 km. Therefore, the value of L indicates the point at which a specific field line crosses the magnetic equator, measured in Earth radii, as illustrated in Figure 4.

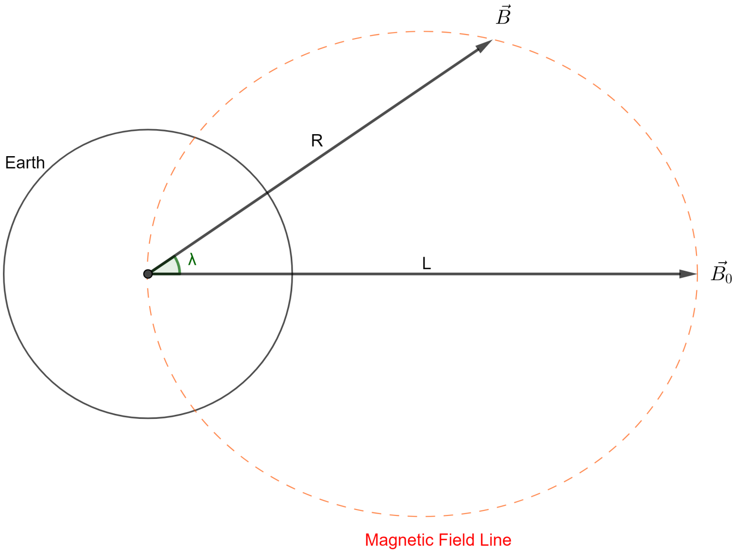

Figure 4. Coordinates for a point in space, given by B and L or R and λ.

The magnitude B of the geomagnetic field, on the other hand, can be calculated as a function of the norm of the magnetic field in the equator, $B_0 = M/L^3$, and the magnetic latitude, λ:

$$\frac{B}{B_0} = \frac{\sqrt{4 - 3cos^2\lambda}}{cos^6\lambda} \tag{4}$$

Thus, the map of the flux of particles in space can be constructed as a function of two coordinates, B and L, which are calculated from the spatial coordinates R and λ.

2.3. Model of the Van Allen Belts

The computation of the radiation fluxes in the mission involves the use of the model of the Van Allen belts, which was accomplished in the present work by dividing them into an inner belt composed only of protons and an outer belt composed only of electrons. Both were modeled by dividing the belts into a series of regions with fixed proton/electron fluxes. Using this approach, the next step was to calculate the radiation fluxes absorbed by the spacecraft, by computing the total time it spends in each region of the proton electron belts. Finally, the resulting radiation fluence is obtained.

Figure 5 presents the model of the Van Allen Belts as in Spenvis [9], in which data of the space missions (AP8 and AE8) are used for the spatial modeling of the omnidirectional integral flux of protons and electrons. The threshold energy used in this model is 10 MeV for protons and 1 MeV for electrons.

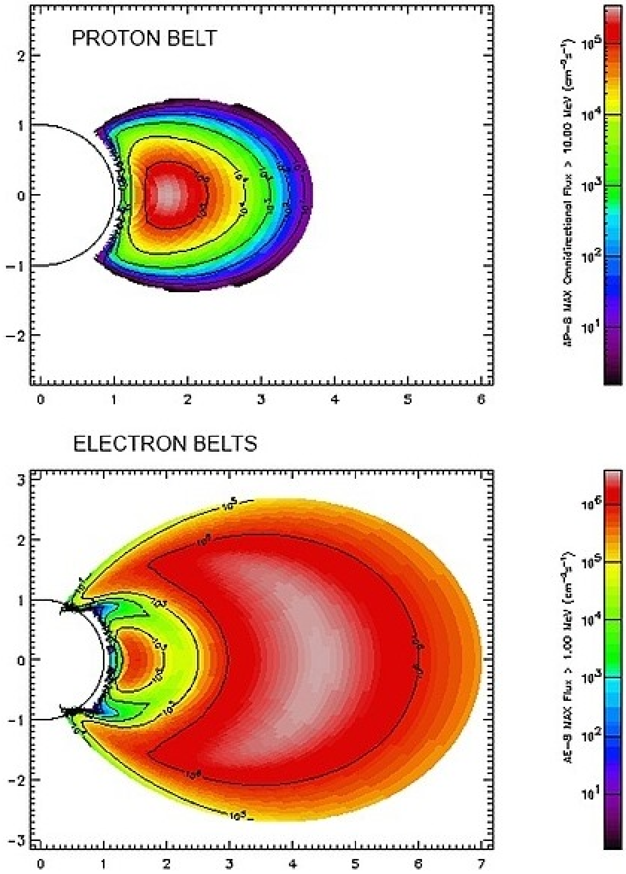

Figure 5. Example of a model for the Van Allen Belts; axes x and y are measured in Earth radii, 6378 km [9].

An analogous model was developed in Matlab through an algorithm in C made by NASA [10], which used data from space missions to calculate the omnidirectional integral flux in each point of space, with a chosen threshold energy. The algorithm was optimized and provided the values of the proton flux, electron flux, B/B_0 and L for a given point inside the Van Allen Belts with polar coordinates: distance from the center of the Earth R and the magnetic latitude λ. The threshold energy chosen was 0.15 MeV for electrons and 4.0 MeV for protons, representing relatively permissive values that allow a more conservative analysis.

Figure 6 presents the contour maps made for the proton and electron belts, in which the omnidirectional integral fluxes of protons are mapped, in particles/(cm^2 s), for each point of space.

Using the results discussed above, the radiation belt models were then used, together with an extensive program for low-thrust transfer orbit optimization, described in [11]. This initial optimization of the trajectory was used to obtain the fluences of protons and electrons as a function of the mission time, considering a non-inclined orbit with respect to the final orbit flying by the Moon [12]. An example is illustrated in Figure 7.

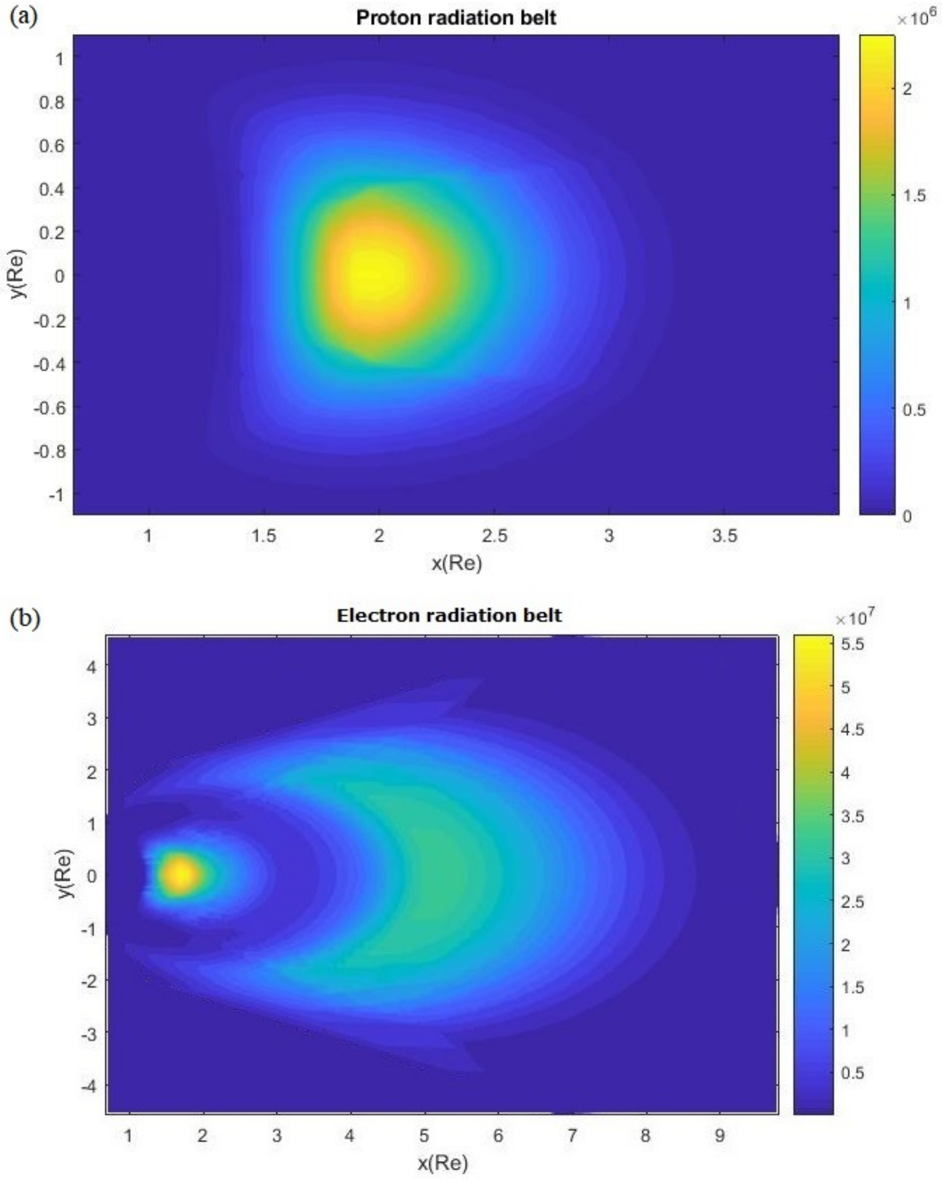

Figure 6. Contour map of the omnidirectional integral flux of: (**a**) protons, (**b**) electrons; *Re* = 6378 km [12].

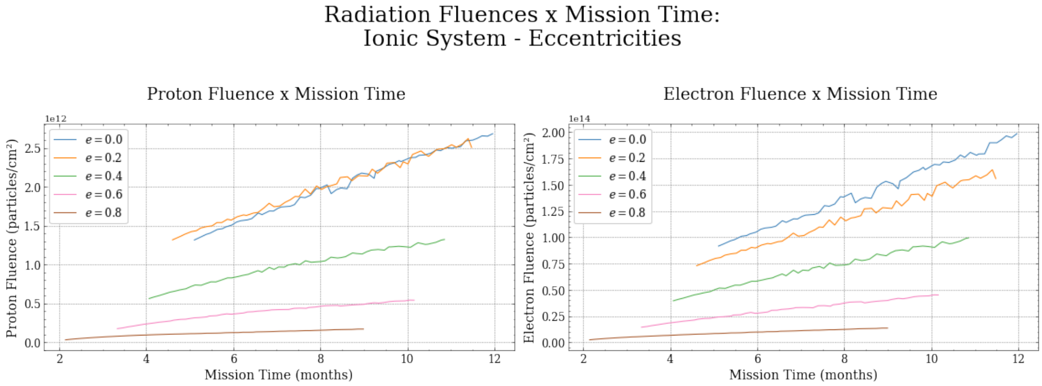

Figure 7. Fluence of protons and electrons as a function of mission time, considering a non-inclined orbit with initial perigee height of 600 km and a propulsion system with $T = 72$ mN and $I_{sp} = 2700$ s.

2.4. Dynamics of the Earth's Magnetic Axis

Given these static models of the Earth's magnetic field, the next step was to explore the dynamics of the Earth's magnetic axis in order to compute trajectories during different periods of time, each of them of a specific inclination.

The first step was to use the Julian date to calculate the universal time, given by the number of Julian centuries after 1 January 2000, 0:00 ET [13]:

$$T = (JD - 2,451,545.0)/36,525 \tag{5}$$

where JD is the Julian date according to the chosen date as an initial parameter.

Next comes the physical parameters of the Moon and the Earth on the day chosen by the mission analyst. The mean longitude of the ascending node of the lunar orbit with respect to the ecliptic and the obliquity of the ecliptic with respect to the Earth's equator were obtained [14] as:

$$\Omega_{moon} = 259.1833 - 1934.13626T + 0.002T^2 + 2.22 \times 10^{-6}T^3 \tag{6}$$

$$\epsilon_{earth} = 23.4393 - 0.013T - 1.64 \times 10^{-7}T^2 + 5.04 \times 10^{-7}T^3 \tag{7}$$

The inclination of the Moon with respect to the ecliptic is the constant $i_c = 5.1453964°$ [15]. Figure 8 illustrates this angle, together with the inclination of the lunar orbit with respect to the Earth's equator, which will be hereafter denoted as i_{moon}.

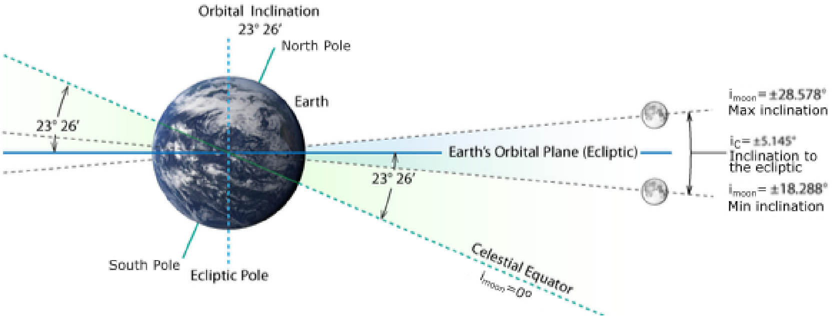

Figure 8. Maximum and minimum inclination of the lunar orbit with respect to the Earth's celestial equator i_{moon}.

Finally, the inclination of the lunar orbit with respect to the Earth's equator, i_{moon}, was calculated [15] based on the three aforementioned parameters:

$$cos(i_{moon}) = cos(i_c)cos(\epsilon_{earth}) - sin(i_c)sin(\epsilon_{earth})cos(\Omega_{moon}) \tag{8}$$

2.5. Statistical Analysis

Using the results obtained from the radiation plots, a multi-linear regression with analysis of variance (ANOVA) was carried out, relating the two final parameters of interest (proton and electron fluence) with the following initial parameters: height of perigee (h_p), eccentricity (e), propulsion system (T and I_{sp}) and the moon's orbit inclination to the Earth's equator i_{moon}. The model started out as a multi-linear regression, given the nature of the trends observed in the plots that will be presented in Section 3, in which several variables seemed to have a linear relationship with respect to the radiation fluences.

A second analysis was also conducted both for protons and electrons, including two of the final parameters computed by the program—mission time (t) and final spacecraft mass (m)—in the regression, since this might be of interest to mission analysts in order to foresee how the mission time and cost will affect the safety parameters (radiation standards).

Starting with the electron fluence, the statistics from the regression are shown in Table 1, first including the final parameters (mass and time), and then excluding them. One can note that both the R-squared and the adjusted R-squared values increase with the addition of both parameters, which justifies their inclusion into the analysis. The significance of the test is also justified by the high value of the F-statistic shown in Table 2. Here (and hereafter), the null hypothesis is that the regression does not fit the data properly, while having a high value for F and t-statistics, as well as low p-values, meaning that we can confidently reject the null hypothesis.

Table 1. Regression statistics for electron fluence, first considering all parameters and then excluding the final mass and mission time.

Regression Statistic	7 Parameters	5 Parameters
Multiple R	0.90	0.86
R-squared	0.81	0.75
R-square adjusted	0.80	0.75
Standard error	2.9×10^{11}	3.3×10^{11}
Observation count	928	928

Table 2. ANOVA for electron fluence.

	gl	SQ	MQ	F	p-Value
Regression	7	3.2×10^{26}	4.6×10^{25}	545.0	0
Residual	920	7.7×10^{25}	8.4×10^{22}		
Total	927	4.0×10^{26}			

Next, a multilinear regression was developed from the seven parameters, which resulted in the following equation with coefficients a_0 to a_7:

$$f_{el} = a_0 + a_1 \mid \vec{T} \mid + a_2 I_{sp} + a_3 h_p + a_4 e + a_5 i_{moon} + a_6 t + a_7 m \tag{9}$$

The uncertainties in each coefficient and their significance tests are shown in Table 3. It can be noted that all parameters have an associated p-value inferior to 0.01, except for the final mass.

Table 3. Regression coefficients for the electron fluence.

	Coefficient	Standard Error	t-Statistic	p-Value
Intersection	5.6×10^{12}	3.7×10^{11}	15.4	1.3×10^{-47}
$\mid \vec{T} \mid$ (mN)	1.0×10^{10}	2.3×10^{09}	4.5	6.4×10^{-06}
I_{sp} (s)	-1.6×10^{09}	3.5×10^{08}	-4.6	5.5×10^{-06}
h_p (km)	-1.3×10^{08}	1.4×10^{07}	-9.4	5.8×10^{-20}
e	-2.0×10^{12}	2.5×10^{11}	-8.3	5.3×10^{-16}
i_{moon} (degrees)	-1.2×10^{11}	3.2×10^{09}	-36.8	2.6×10^{-183}
t (months)	6.5×10^{10}	1.1×10^{10}	5.8	7.0×10^{-09}
m (kg)	1.0×10^{10}	7.6×10^{09}	1.3	1.9×10^{-01}

Proceeding with the proton fluence, the regression statistics are shown in Table 4, first including the final parameters (mass and time), and then excluding them. One can notice, as was the case for the electron fluence, that both the R-squared and the adjusted R-squared values increase with the addition of both parameters, which justifies their inclusion in the analysis. The significance of the test is also justified due to the high value of the F-statistic shown in Table 5.

Table 4. Regression statistics for proton fluence, first considering all parameters and then excluding the final mass and mission time.

Regression Statistic	7 Parameters	5 Parameters
Multiple R	0.92	0.82
R-squared	0.84	0.68
R-square adjusted	0.84	0.67
Standard error	1.6×10^{13}	2.2×10^{13}
Observation count	928	928

Table 5. ANOVA for proton fluence.

	gl	SQ	MQ	F	p-Value
Regression	7.00	1.2×10^{30}	1.7×10^{29}	697.8	0
Residual	920.00	2.3×10^{29}	2.5×10^{26}		
Total	927.00	1.4×10^{30}			

Next, a multilinear regression was developed from the seven parameters, which resulted in the following equation with coefficients b_0 to b_7:

$$f_{pro} = b_0 + b_1 \mid \vec{T} \mid + b_2 I_{sp} + b_3 h_p + b_4 e + b_5 i_{moon} + b_6 t + b_7 m \quad (10)$$

The uncertainties in each coefficient and their significance tests are shown in Table 6. It can be noted that all parameters have an associated p-value inferior to 0.01.

Table 6. Regression coefficients for the proton fluence.

	Coefficient	Standard Error	t-Statistic	p-Value
Intersection	2.0×10^{14}	2.0×10^{13}	10.0	2.7×10^{-22}
$\mid \vec{T} \mid$ (mN)	8.1×10^{11}	1.2×10^{11}	6.6	9.2×10^{-11}
I_{sp} (s)	-1.3×10^{11}	1.9×10^{10}	−6.6	5.4×10^{-11}
h_p (km)	-9.3×10^{09}	7.7×10^{08}	−12.1	2.2×10^{-31}
e	-1.7×10^{14}	1.3×10^{13}	−12.6	1.2×10^{-33}
i_{moon} (degrees)	-3.8×10^{12}	1.7×10^{11}	−21.7	6.3×10^{-85}
t (months)	5.6×10^{12}	6.0×10^{11}	9.3	1.0×10^{-19}
m (kg)	1.8×10^{12}	4.1×10^{11}	4.2	2.4×10^{-05}

2.6. Machine Learning Regression

In order to improve the model efficiency, a machine learning (ML) approach using supervised algorithms was also carried out, together with the linear regression. The ML approach is modeled as a supervised learning problem, that is, a structure tailored to explore and extract potential relationships between the input variables and the output target variables, using a subset of our data so that the system can learn from itself. Usually, this relationship is nonlinear and cannot be explicitly formulated.

The first method selected for a non-linear attempt at fitting the data were support vector machines (SVMs). SVM is a machine learning technique that can work very similar to the ordinary least squares method—that is, the model works by fitting a curve to the data in such a way that the points are distributed in the closest way possible to the model. Nevertheless, to provide an expressive improvement on the linear regression that had already been conducted, the specific SVM method used to fit the regression was the radial-based functions (RBF) method, which penetrates more deeply than a simple linear fit. More details about SVMs using RBF can be found in [16].

Going into detail, the artificial neural network (ANN) itself is an ML algorithm that is capable of approximating smooth functions to a regression using adequate neurons and layers. As suggested by the name, several neurons are linked in a network, as illustrated in Figure 9. Each of them is called a node, which acts upon the next set of neurons, called a layer. The input layer comprises our input data of x variables (h_p, e, T, I_{sp}, i_{moon}, t, m), whereas the output layer is a single y variable (f_{el} or f_{pro}). Scalar gains, K_{ij}, are placed between each neuron output and neuron input, which are optimized by the algorithm after providing the training data (input x and output y for supervised learning) and minimizing the cost function defined as the mean square error (MSE):

$$MSE = \frac{1}{N}\sum_{i=1}^{N}(y_i - \hat{y}_i)^2$$

where N is the training data size, $\hat{y}_i$ is the ANN's i-th output and y_i indicates the target data themselves.

Finally, the hidden layers add extra complexity to the system, not only through adding more gain parameters between them, but also through the use of activation functions in each of them, which can be thought as mathematical filters between the input and the output layers. Two popular activation functions are the hyperbolic tangent (Tanh) function and the rectified linear unit (ReLU). Both the number of neurons and layers, however, will affect the complexity of the network in an exponential fashion; therefore, each of these hyperparameters, along with the activation function and the number of iterations (the number of times the algorithm will train itself), must be carefully chosen to reach an optimum value [17].

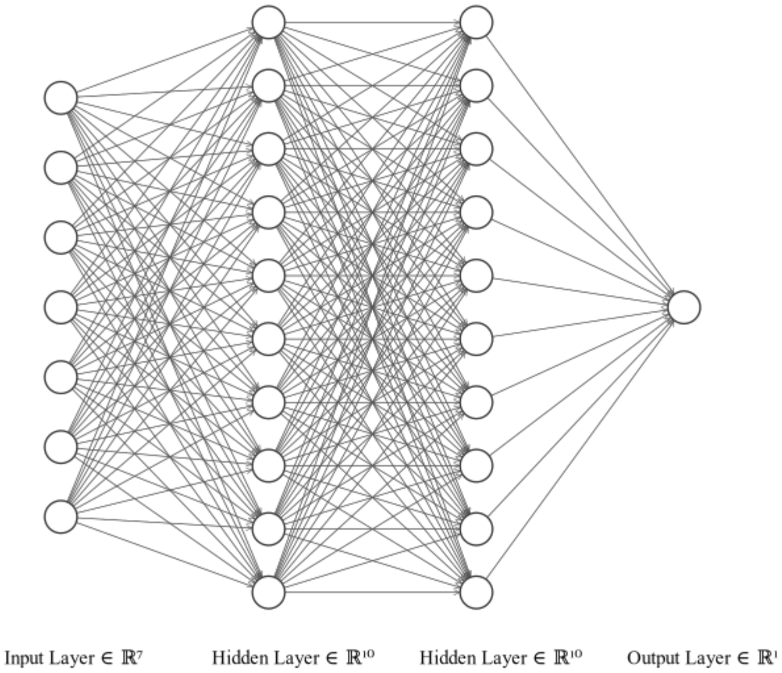

Figure 9. Neural network with two hidden layers of 10 neurons.

After training the ML model, a hidden relationship might be uncovered if the model's performance is good (that is, if the trained models are well suited on testing data). Nevertheless, in the case that the performance is not as good as expected, there is no way to reach the conclusion that there is such a relationship [18]. Therefore, when working with ML algorithms, a few important steps should be taken into account to fit the very best model to our data, namely:

1. Feature scaling, which prevents our model from overestimating a specific feature due to its order of magnitude;
2. Data pipelines, which are a good practice for parallel computing and for the optimization of processing time;
3. Performance comparison, which confirms that the chosen ML algorithm is indeed a good option against others;
4. Hyperparameter optimization, which guarantees a better fit, given the chosen model.

Before applying each of the five steps above, however, an initial attempt via neural networks was carried out with Python's Scikit-learn kit [19]. The scaler used was the MinMaxScaler; no pipeline was constructed; no other algorithm was used at the same time and the hyperparameters (two hidden layers of 10 neurons, 100 iterations and the Relu activation function) were not optimized. Despite being a crude version, this model already proved to be valuable: the neural network resulted in a mean squared error of only 0.0058 and an R^2 of 0.875. Hence, the improvements above were made on top of this model.

Based on the initial attempt, the first step was processing the data through a pipeline, which was accomplished using Scikit-learn's `sklearn.pipeline.Pipeline` class. The importance of this procedure is "to assemble several steps that can be cross-validated together while setting different parameters" [20]. In other words, it is a way to centralize every step of the machine learning algorithm inside a single object, which not only organizes the algorithm, but also avoids leaking from the training data to the testing data.

Next, the scaler used was improved for our specific case, together with a comparison with other two models—Scikit-learn's linear regressor and support vector machine regressor. Each scaler uses a different mathematical method and hence should be used in a specific statistical distribution of our data. Scikit-learn's StandardScaler should be used when a feature is approximately normally distributed, whereas the MinMaxScaler preserves the shape of the feature, for instance. Based on the comparison shown in Table 7, the StandardScaler together with the ANN resulted in better statistics and hence this was chosen as the pair to be used.

Table 7. Scaler and model comparison for three regression methods. It is clear that the linear regression was improved by the use of non-linear ML models.

Scaler	Method	R-Square	MSE
MinMax	Linear Regression	0.815	0.0086
MinMax	Support Vector Machine	0.931	0.0032
MinMax	Neural Network	0.962	0.0018
Standard	Linear Regression	0.815	0.0086
Standard	Support Vector Machine	0.926	0.0034
Standard	Neural Network	0.977	0.0011

Finally, the hyperparameters from the ANN were optimized using Scikit-learn's GridSearchCV function. This method searches for the model that yields the best results from a discrete set of values to each hyperparameter. In this case, the activation function, the maximum number of iterations and the number of neurons in each layer were chosen from the following values, respectively: (Identity, Logistic, Tanh, Relu), (10, 50, 100), (10, 20, 40, 60, 80, 100). Each combination of these hyperparameters resulted in different statistics; the best being the Relu activation function with 100 maximum iterations and a batch size of 10. A summary of the set of improvements and their respective results is shown in Table 8.

Table 8. Summary of the improvements made in the ANN model.

Improvement	R-Squared	MSE
None	0.875	0.0058
Pipeline	0.966	0.0016
Scaling	0.977	0.0011
Hyperparameter Optimization	0.997	0.0002

2.7. Lunar Swing-By

A gravity-assisted maneuver, or swing-by, is a technique that has been progressively gaining ground since it was first executed by the Soviet spacecraft Luna-3 in 1957. Such growth can evidenced by the number of missions that have flown or are scheduled to fly using this technique. A successful example is the Voyager missions, which flew to the outer planets of the solar system using successive swing-bys on the visited planets, thus gaining the energy to proceed with the mission [21].

In particular, the use of the moon in gravity-assisted maneuvers has been demonstrated numerous times. In the simplest case, one can use the technique to launch a spacecraft into an elliptical or hyperbolic orbit that ends up escaping from Earth [22]. Another very practical case is the use of successive swing-bys with the Moon to obtain desirable geometries in spacecraft orbits around the Earth, such as satellites that observe solar phenomena, as seen in [23]. Figure 10 shows one such example.

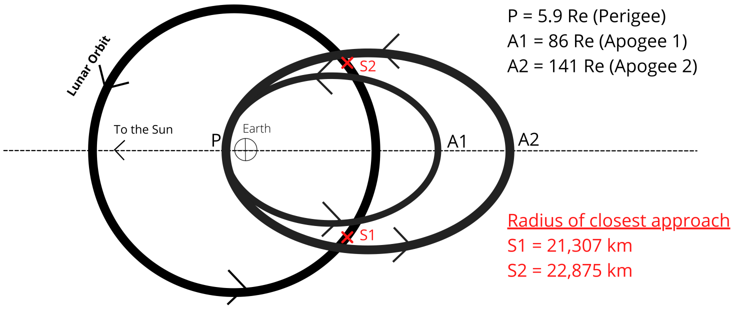

Figure 10. Use of successive swing-bys with the moon in the ISEE-3/ICE comet mission [23].

For a study with simplified modeling, we can assume that the whole mission can be divided into several steps. The simple two-body model is used for each of these steps, based on [24,25]. This approach is usually called patched conics. The system is composed of three bodies: M1, a massive body in the center of the Cartesian system; M2, a smaller body, planet or satellite of M1 in a Keplerian orbit around M1; and M3, a spacecraft with infinitesimal mass or a particle that is traveling in a generic orbit around M1 when it makes an encounter with M2. This encounter alters the orbit of M3, and the whole phenomenon is called a swing-by maneuver. According to these hypotheses, the orbits of M1 and M2 do not change. In the present case, we assume that M1 is the Earth, M2 is the moon and M3 is the spacecraft.

We want, therefore, to study the effects of a lunar swing-by on the orbit of a spacecraft that has elevated its spiral trajectory using low thrust, passing through the Van Allen belts in the process. The fundamental metrics that will be described to quantize these effects are the following: the increment in velocity, or ΔV, and the increment in energy, or ΔE. More details on their derivation can be found in Appendix A.

3. Results

Varying the mission date and, hence, the relative inclination of the Earth's magnetic field, several results could be obtained using the calculations described above. The program ran with the initial spacecraft mass of $m = 160$ kg (this mass was assumed for the Brazilian low-thrust Aster mission to the (153591) 2001 SN263 triple asteroid) and a final orbital energy equal to zero. The following five initial conditions were chosen: thrust T and specific impulse I_{sp} of the propulsion system, perigee altitude h_p, eccentricity e and the inclination of the moon's orbit to the Earth's equator i_{moon}, the latter three with respect to the initial orbit. For the study of the lunar swing-by in isolation, another initial condition was considered—the maximum approach distance during the encounter between the spacecraft and the moon, R_p.

First, in order to test significant variations in the parameter of inclination of the lunar orbit, the following dates were chosen: 1 January 2016 ($i_{moon} = 18°$), 1 June 2012 ($i_{moon} = 21°$), 1 January 2011 ($i_{moon} = 24°$), 1 October 2009 ($i_{moon} = 26°$) and 1 January 2006 ($i_{moon} = 28°$). Second, four propulsion systems were considered, the first one being the ionic system ($T = 72$ mN and $I_{sp} = 2700$ s); the second one being NASA's Evolutionary Xenon Thruster (NEXT), with $T = 236$ mN and $I_{sp} = 4190$ s; the third one being the BHT-8000 (an 8 kW Hall Effect thruster), with $T = 449$ mN and $I_{sp} = 2210$ s; and the fourth one being the PPS-1350 (a 1350 W Hall Effect thruster), with $T = 90$ mN and $I_{sp} = 1660$ s. Third, two values for altitude of perigee were chosen, namely 600 km and 2209 km, as a means to yield expressive differences in the final parameters. Five initial eccentricities were chosen: e = 0; 0.2; 0.4; 0.6; 0.8. Finally, five values were stipulated for the approach distance to the moon. These values were chosen as 110% to 150% of the lunar radius, in increments of 10%: $R_p = 1910.7, 2084.4, 2258.1, 2431.8$ and 2605.5 km.

The final parameters are as follows: total mission time t, in months; final mass m of the spacecraft, in kg; gain in speed after the swing-by ΔV, in km/s; energy gain after the swing-by ΔE, in km^2/s^2; and the fluence of protons f_{pro} and of electrons f_{el}, once the trajectory is complete, in particles/cm^2.

3.1. Radiation vs. Time

Figure 11 shows the fluences of protons and electrons as a function of the total mission time, for the five initial eccentricities chosen (0; 0.2; 0.4; 0.6; 0.8) and considering the NEXT propulsion system ($T = 236$ mN and $I_{sp} = 4190$ s), $h_p = 600$ km and $i_{moon} = 18°$. Analogous plots were made for radiation vs. mission time and are shown in Figures 12–14, but this time changing other parameters instead of the eccentricity, namely, the propulsion system, inclination and the height of the perigee.

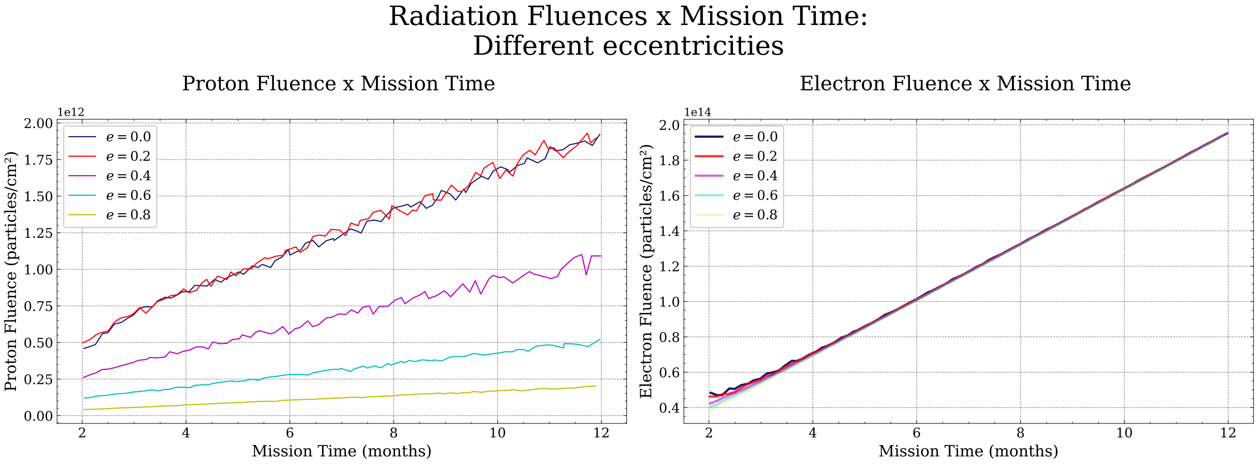

Figure 11. Particle fluence as a function of mission time for the five initial eccentricities chosen (0; 0.2; 0.4; 0.6; 0.8) and considering the NEXT propulsion system ($T = 236$ mN and $I_{sp} = 4190$ s), $h_p = 600$ km and $i_{moon} = 18°$.

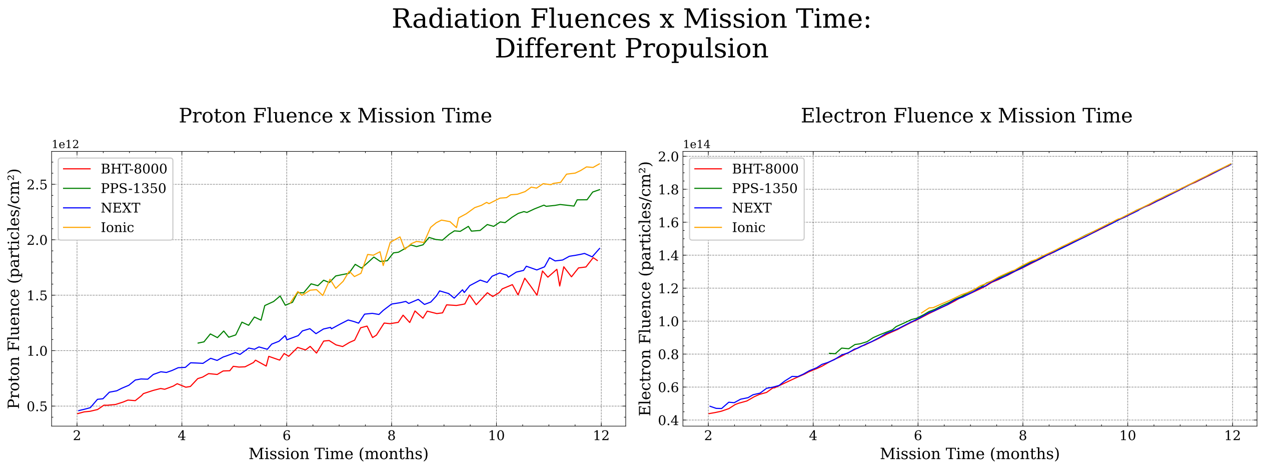

Figure 12. Particle fluence as a function of mission time for the four chosen propulsion systems—NEXT, ionic, BHT-8000 and PPS-1500—and considering an initial orbit with $h_p = 600$ km, $e = 0$ and $i_{moon} = 18°$.

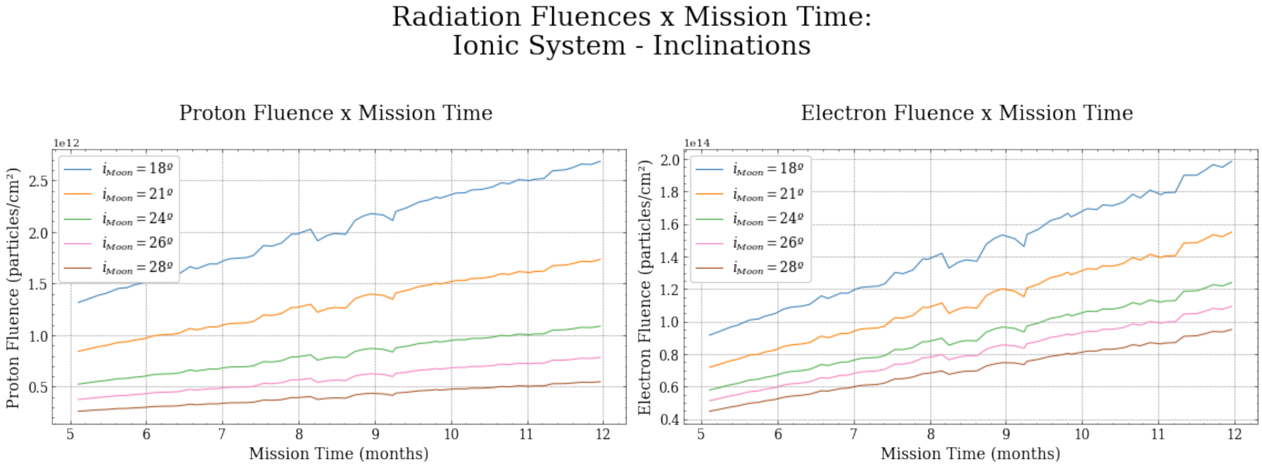

Figure 13. Particle fluence as a function of total mission time for the five chosen lunar inclinations ($i_{moon} = 18°; 21°; 24°; 26°; 28°$), considering a propulsion system NEXT, $h_p = 600$ km and $e = 0$.

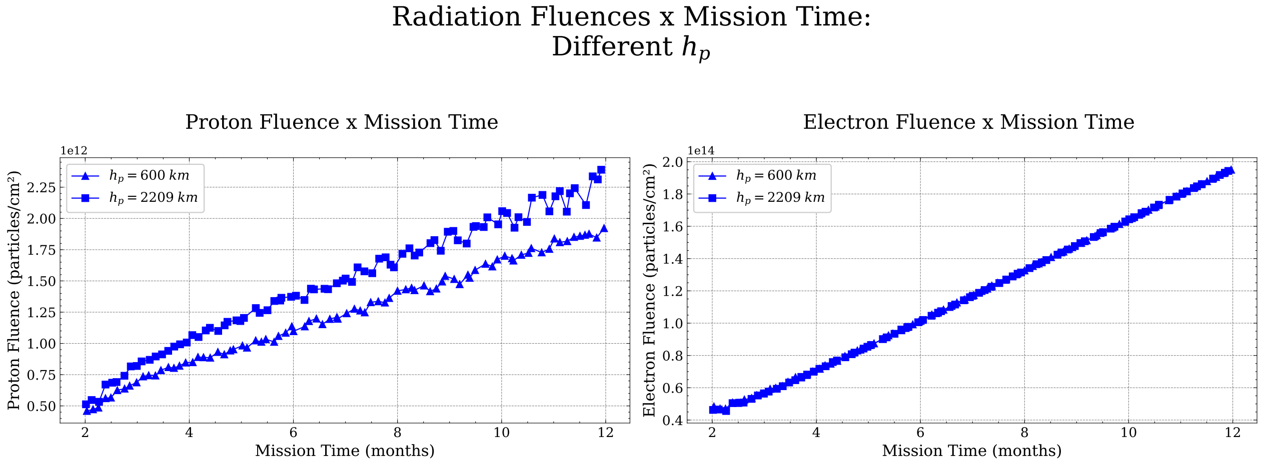

Figure 14. Particle fluence as a function of mission time for the two initial perigee heights chosen ($h_p = 600$ km and $h_p = 2209$ km) and considering the propulsion system NEXT ($T = 236$ mN and $I_{sp} = 4190$ s), with $e = 0$ and $i_{moon} = 18°$.

3.2. *Final Mass* × *Time*

The graph in Figure 15 shows the final mass as a function of the total mission time, for the five initial eccentricities chosen (0; 0.2; 0.4; 0.6; 0.8) and considering the system of propulsion NEXT ($T = 236$ mN and $I_{sp} = 4190$ s), $h_p = 600$ km and $i_{moon} = 18°$. Similarly, Figures 16 and 17 show plots for mass vs. mission time, changing the propulsion system and the height of the perigee instead of eccentricity.

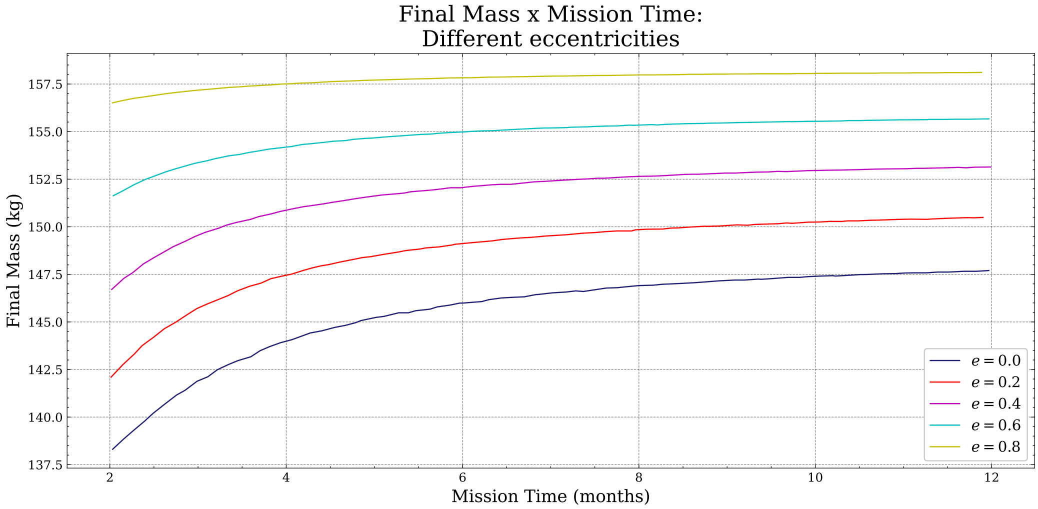

Figure 15. Final mass as a function of mission time for the five initial eccentricities chosen (0; 0.2; 0.4; 0.6; 0.8) and considering the system of propulsion NEXT ($T = 236$ mN and $I_{sp} = 4190$ s), $h_p = 600$ km and $i_{moon} = 18°$.

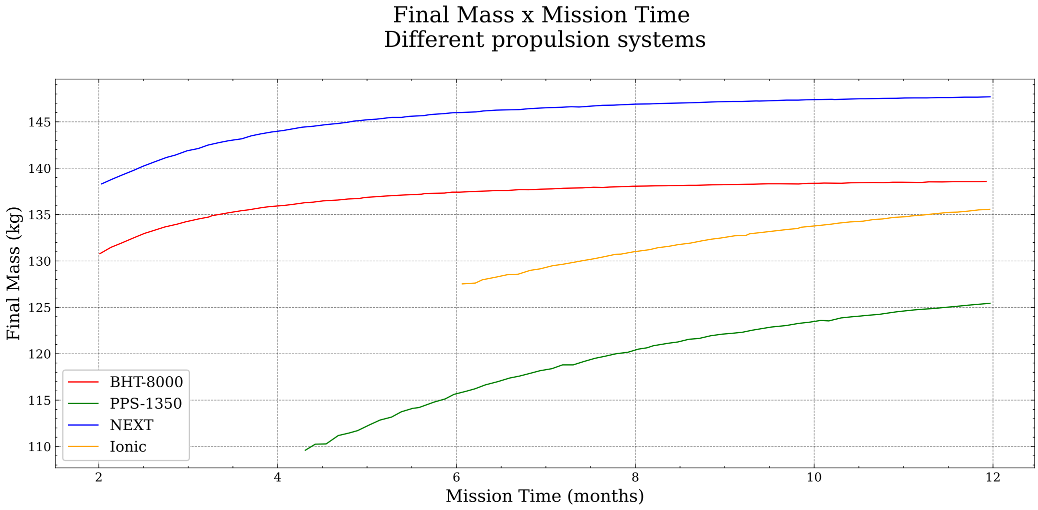

Figure 16. Final mass as a function of mission time for the four chosen propulsion systems—NEXT, Ionic, BHT-8000 and PPS-1500—and considering an initial orbit with $h_p = 600$ km, $e = 0$ and $i_{moon} = 18°$.

3.3. ΔE × *Time*

The graphs in Figure 18 show the increase in energy ΔE in both configurations (ψ_1 and ψ_2) as a function of the total mission time, for the four chosen propulsion systems—ionic, NEXT, BHT-8000 and PPS-1500—and considering an initial orbit with $h_p = 600$ km, $e = 0$, $i_{moon} = 18°$ and a moon approach distance $R_p = 1910.7$ km. Figure 19a–d show the same ΔE vs. mission time plots for each propulsion system separately, varying the parameter of the initial eccentricity. Figures 20 and 21 show analogous plots for the Ionic system, varying the parameters of the height of the perigee and the approximation distance.

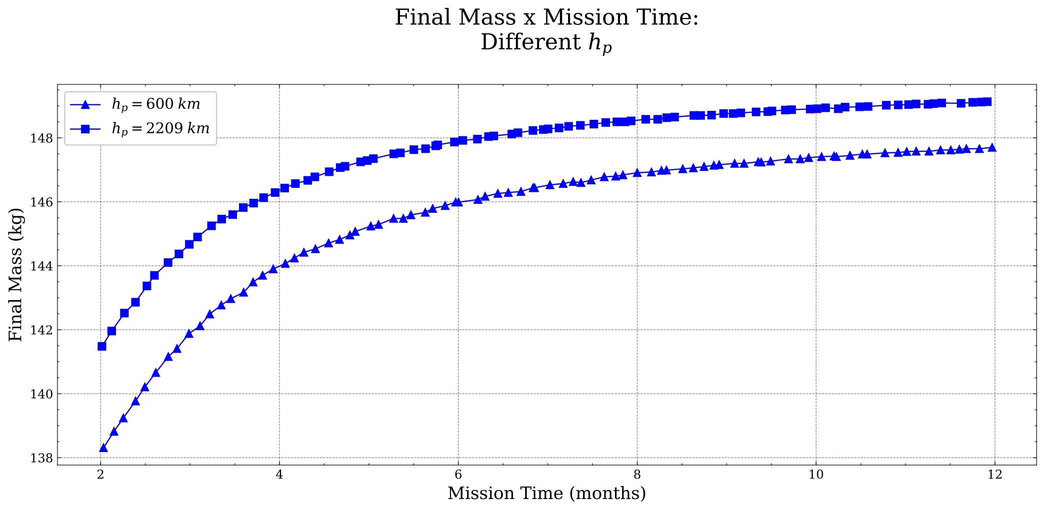

Figure 17. Final mass as a function of mission time for the two initial perigee heights chosen ($h_p = 600$ km and $h_p = 2209$ km) and considering the NEXT propulsion system ($T = 236$ mN and $I_{sp} = 4190$ s), with $e = 0$ and $i_{moon} = 18°$.

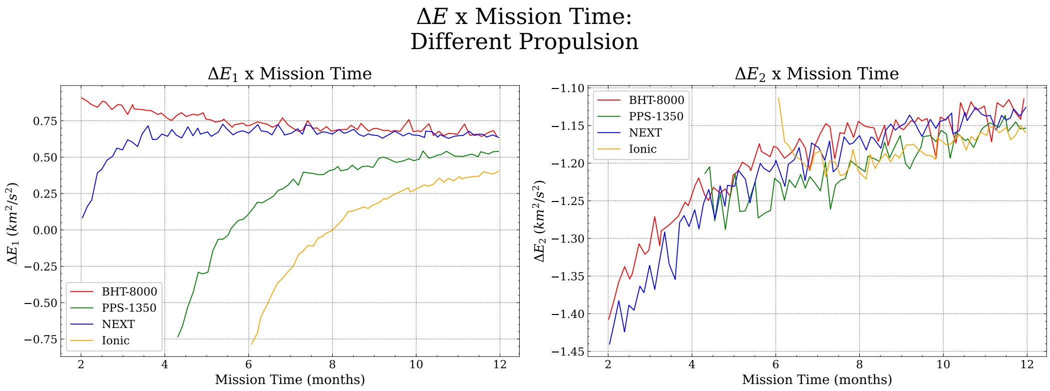

Figure 18. Energy gain, in its two configurations, as a function of mission time for the four chosen propulsion systems—ionic, NEXT, BHT-8000 and PPS-1500—and considering an initial orbit with $h_p = 600$ km, $e = 0$, $i_{moon} = 18°$ and a moon approach distance $R_p = 1910.7$ km.

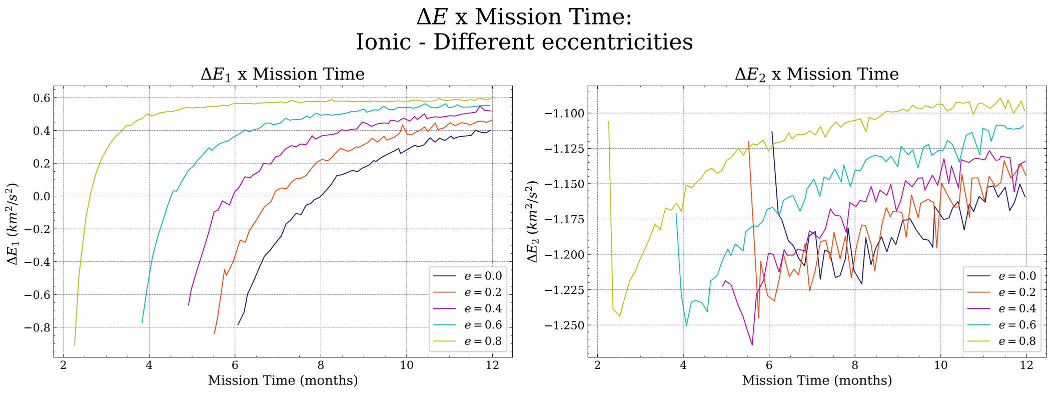

(**a**)

Figure 19. *Cont.*

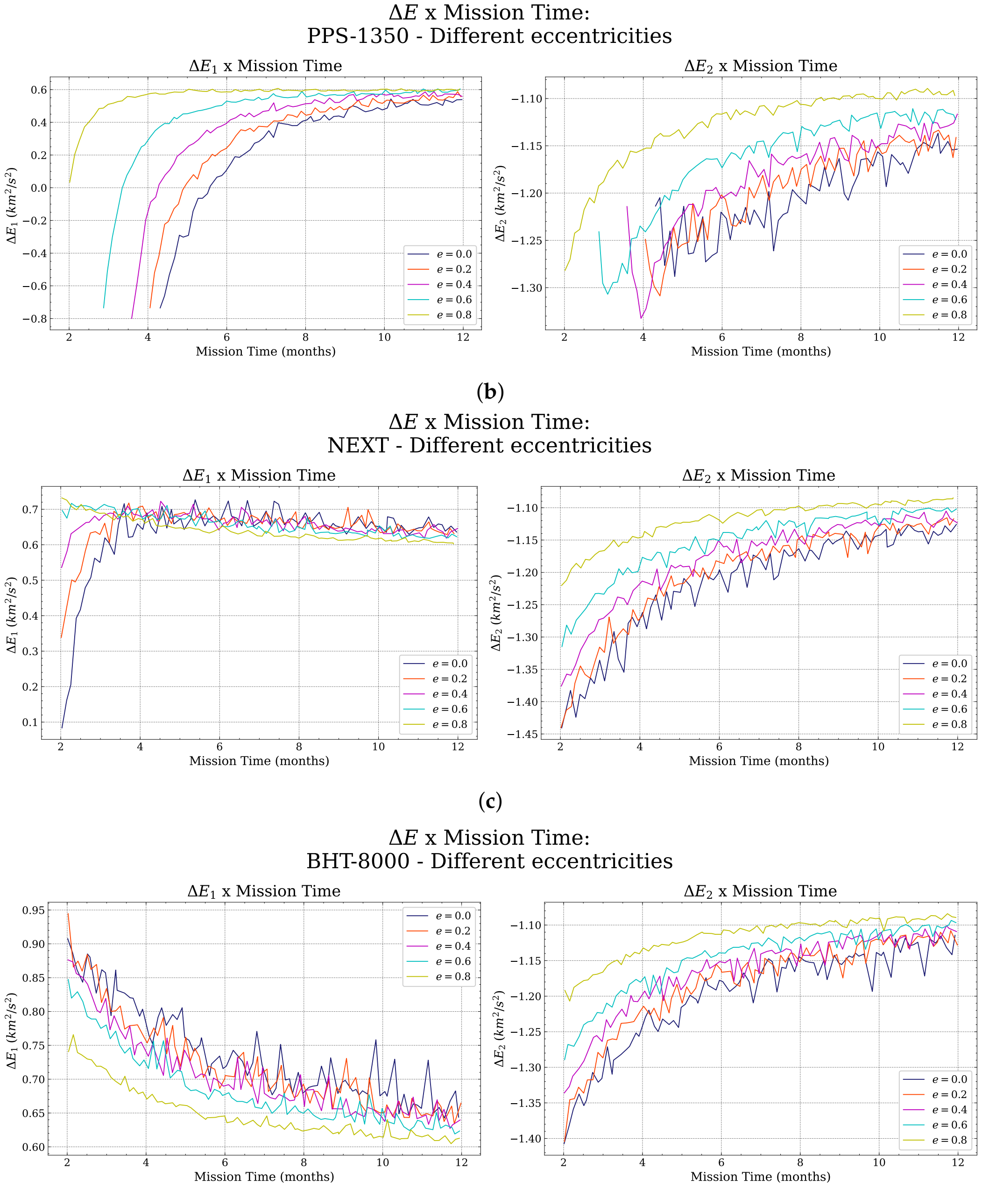

(**b**)

(**c**)

(**d**)

Figure 19. Energy gain, in its two configurations, as a function of mission time for the five initial eccentricities chosen (0; 0.2; 0.4; 0.6; 0.8), $h_p = 600$ km, $i_{moon} = 18^\circ$ and $R_p = 1910.7$ km. (**a**) Ionic propulsion system. (**b**) PPS-1350 propulsion system. (**c**) NEXT propulsion system. (**d**) BHT-8000 propulsion system.

3.4. $\Delta V \times$ Time

The graph in Figure 22 shows the increase in speed ΔV as a function of the total mission time, for the four chosen propulsion systems—ionic, NEXT, BHT-8000 and PPS-1500—and considering the initial parameters as: $h_p = 600$ km, $e = 0$, $i_{moon} = 18^\circ$ and $R_p = 1910.7$ km. Figure 23a–d show the same ΔV vs. mission time plots for each propulsion system separately, varying the parameter of initial eccentricity. Figures 24 and 25, then show analogous plots for the ionic system, varying the parameters of the height of the perigee and the approximation distance, respectively.

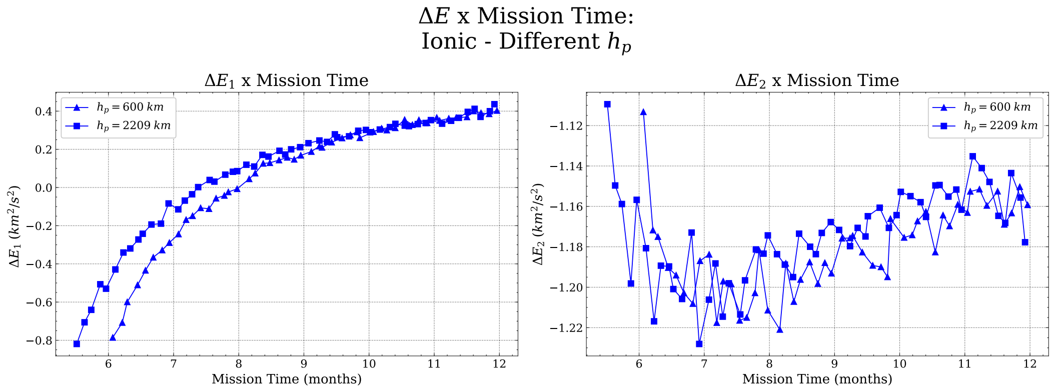

Figure 20. Energy gain, in its two configurations, as a function of mission time for the two chosen initial perigee heights ($h_p = 600$ km and $h_p = 2209$ km) and considering the ionic propulsion system, with $e = 0$, $i_{moon} = 18°$ and $R_p = 1910.7$ km.

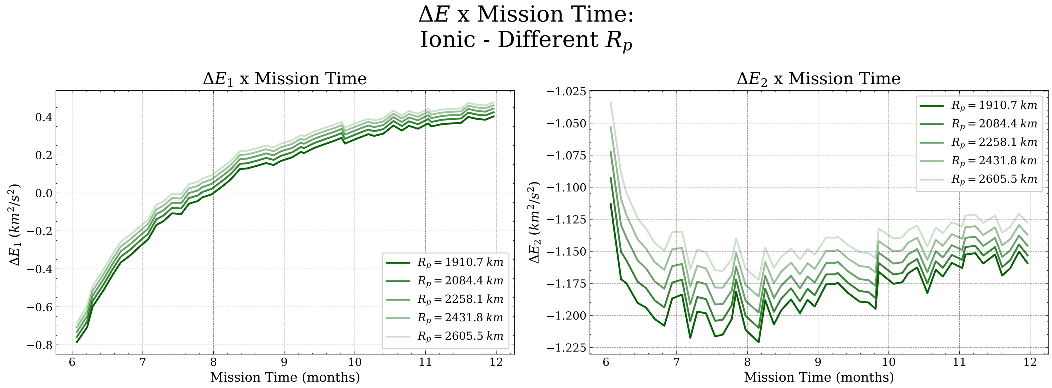

Figure 21. Energy gain, in its two configurations, as a function of mission time for the five approach distances R_p chosen initials (1910.7; 2084.4; 2258.1; 2431.8; 2605.5 km) and considering the ionic propulsion system, $h_p = 600$ km, $e = 0$ km, $i_{moon} = 18°$.

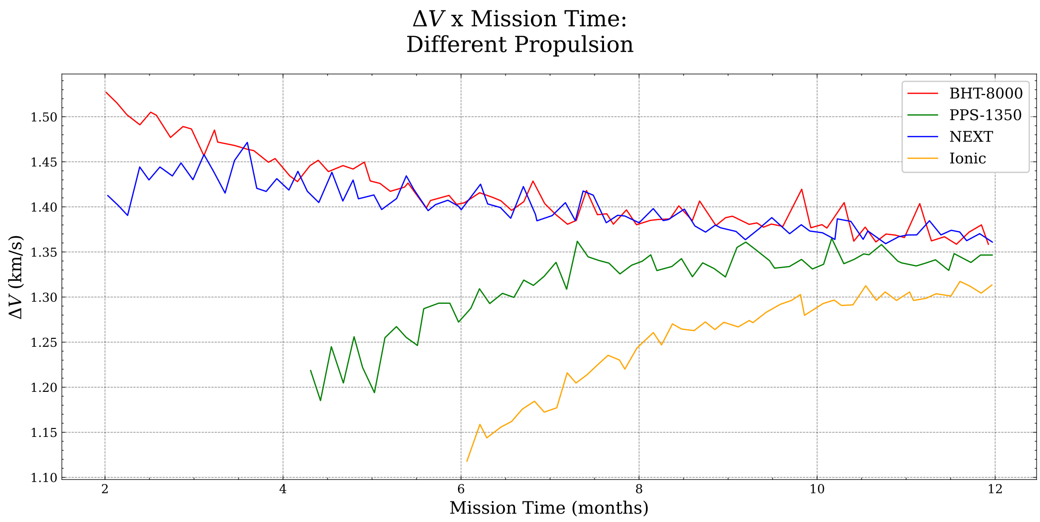

Figure 22. Speed gain as a function of mission time for the four chosen propulsion systems—ionic, NEXT, BHT-8000 and PPS-1500—and considering the initial parameters as: $h_p = 600$ km, $e = 0$, $i_{moon} = 18°$ and $R_p = 1910.7$ km.

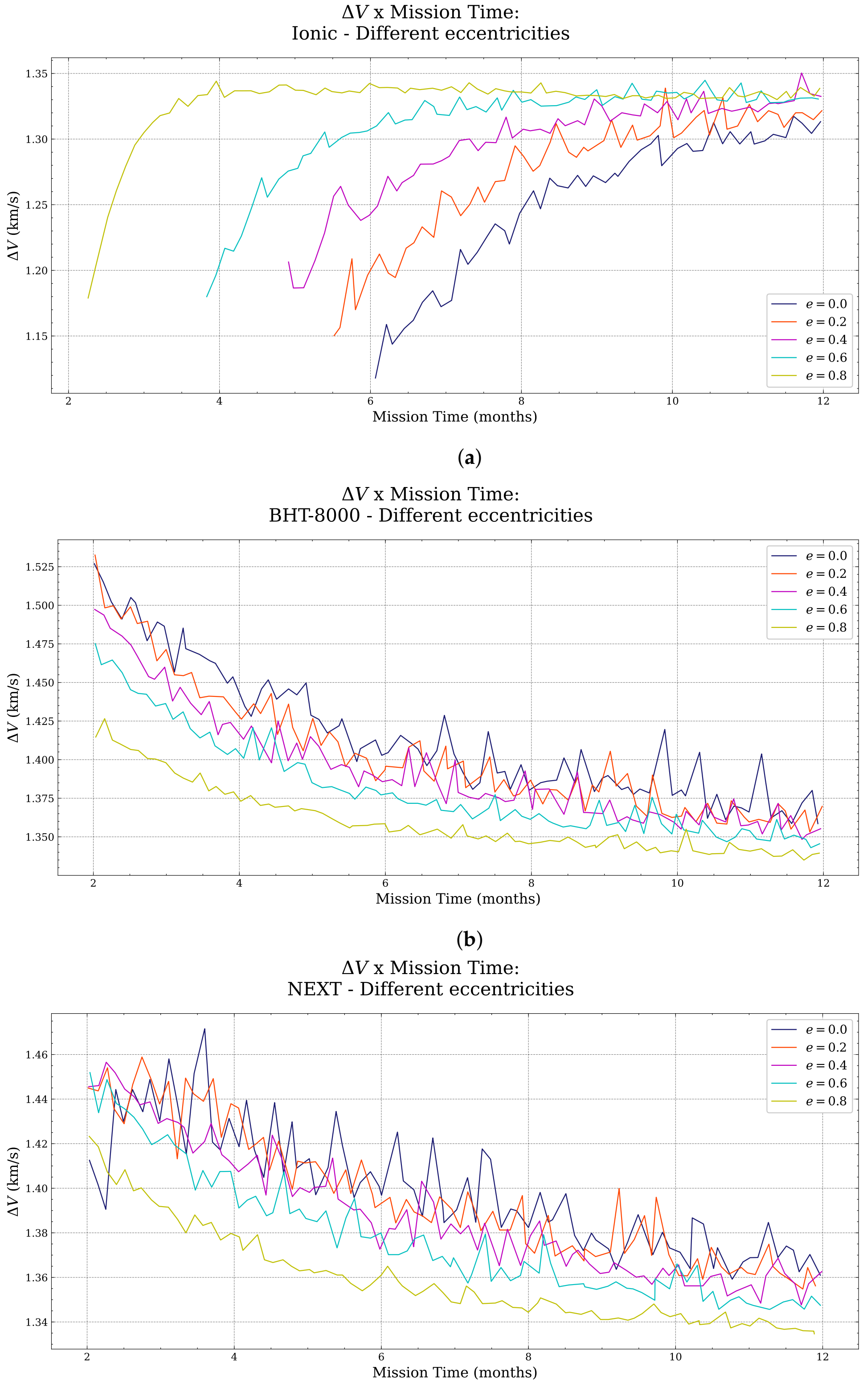

(**a**)

(**b**)

(**c**)

Figure 23. *Cont.*

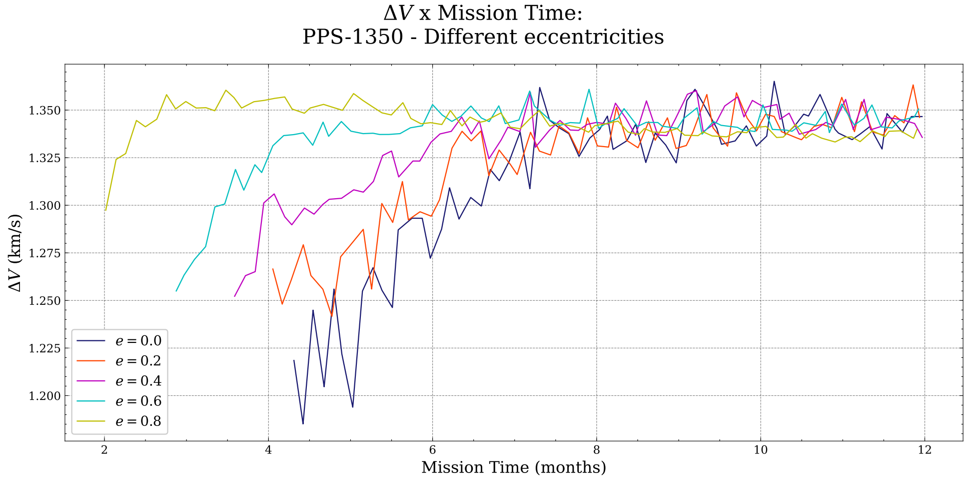

(**d**)

Figure 23. Speed gain as a function of mission time for the five initial eccentricities chosen (0; 0.2; 0.4; 0.6; 0.8), $h_p = 600$ km, $i_{moon} = 18°$ and $R_p = 1910.7$ km. (**a**) Ionic propulsion system. (**b**) BHT-8000 propulsion system. (**c**) NEXT propulsion system. (**d**) PPS-1350 propulsion system.

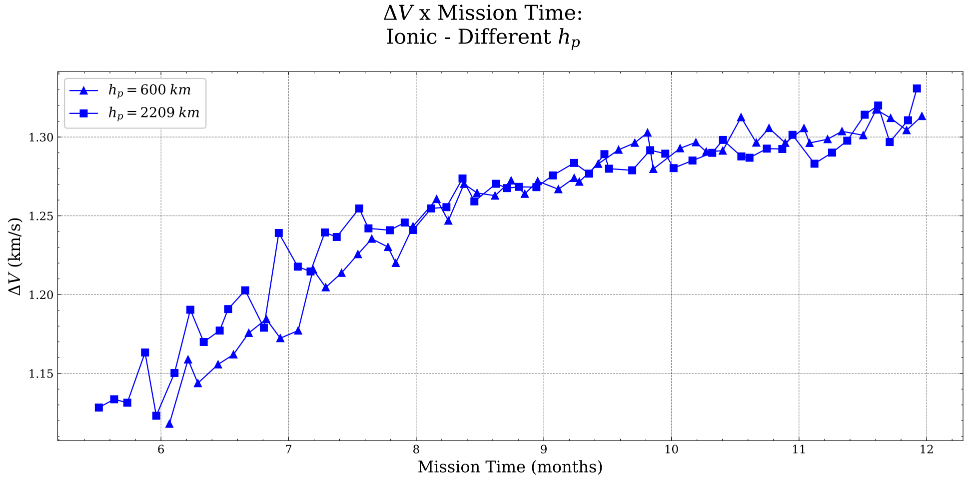

Figure 24. Speed gain as a function of mission time for the two initial perigee heights chosen ($h_p = 600$ km and $h_p = 2209$ km) and considering the ionic propulsion system, with $e = 0$, $i_{moon} = 18°$ and $R_p = 1910.7$ km.

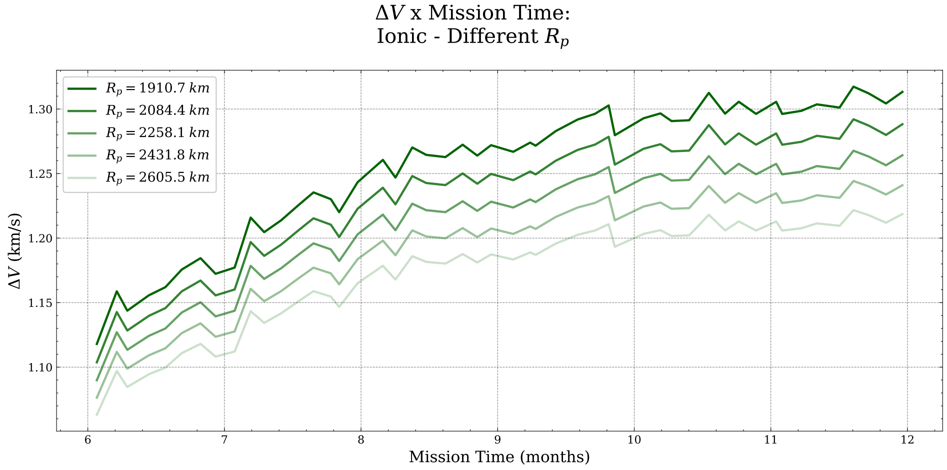

Figure 25. Speed gain as a function of mission time for the five initial chosen approach distances R_p (1910.7; 2084.4; 2258.1; 2431.8; 2605.5 km) and considering the ionic propulsion system, $h_p = 600$ km, $e = 0$ km, $i_{moon} = 18°$.

3.5. $\Delta E \times$ *Mass*

The graph in Figure 26 shows the increase in energy ΔE in both configurations (ψ_1 and ψ_2) as a function of the final mass, where the size of the points represents the fluence value of electrons absorbed by the spacecraft, for the four chosen propulsion systems—ionic, NEXT, BHT-8000 and PPS-1500—and considering an initial orbit with $h_p = 600$ km, $e = 0$, $i_{moon} = 18°$ and a moon approach distance $R_p = 1910.7$ km. Figure 27a–d show the same ΔE vs. final mass plots for each propulsion system separately, varying the parameter of initial eccentricity. Figure 28a–d show analogous plots, but this time varying the height of the perigee. Figure 29, finally, shows ΔE vs. final mass plots, varying the approximation distance.

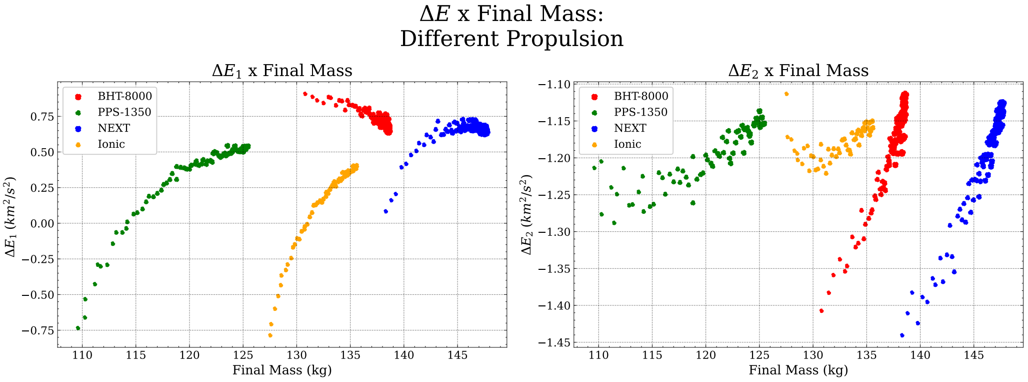

Figure 26. Energy gain, in its two configurations, as a function of the final mass, where the size of the dots represents the electron fluence, for the four chosen propulsion systems—ionic, NEXT, BHT-8000 and PPS-1500—and considering an initial orbit with $h_p = 600$ km, $e = 0$, $i_{moon} = 18°$ and moon approach distance $R_p = 1910.7$ km.

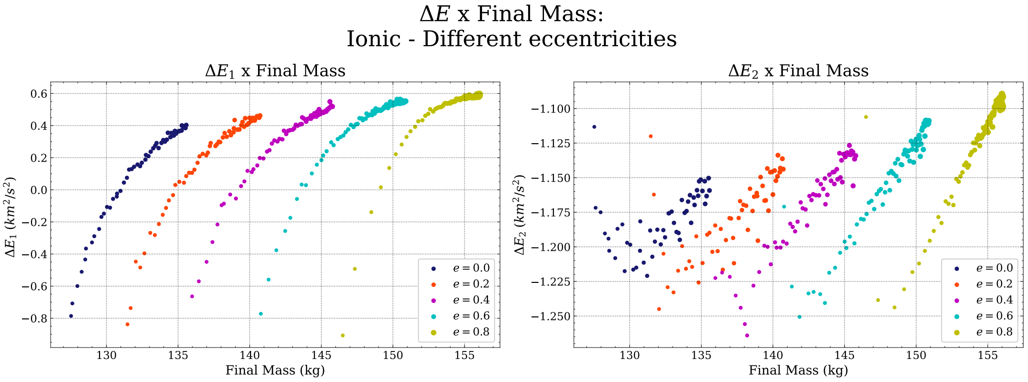

(**a**)

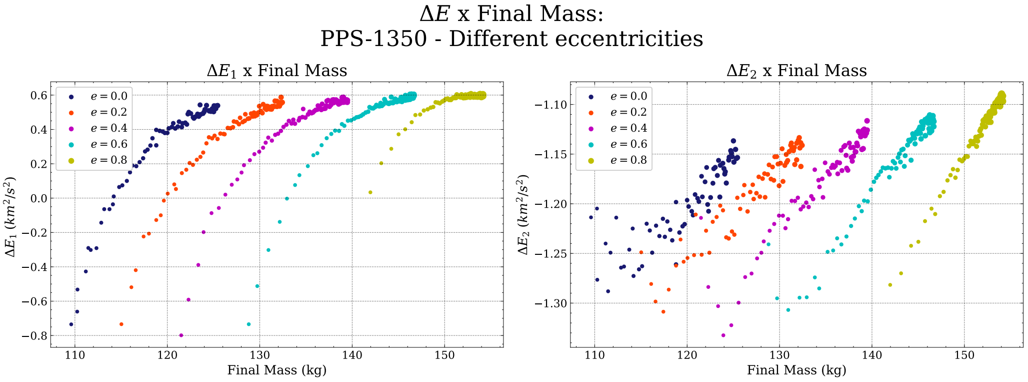

(**b**)

Figure 27. *Cont.*

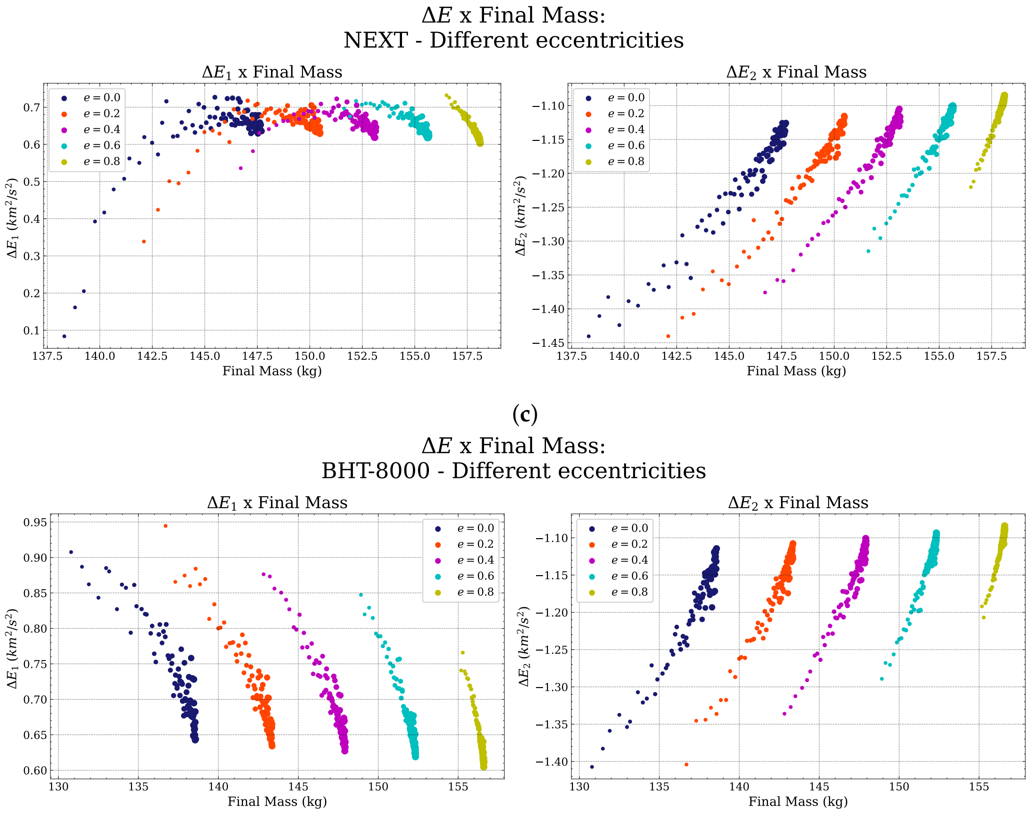

(c)

(d)

Figure 27. Energy gain, in its two configurations, as a function of final mass for the five initial eccentricities chosen (0; 0.2; 0.4; 0.6; 0.8), $h_p = 600$ km, $i_{moon} = 18^\circ$ and $R_p = 1910.7$ km. (**a**) Ionic propulsion system. (**b**) PPS-1350 propulsion system. (**c**) NEXT propulsion system. (**d**) BHT-8000 propulsion system.

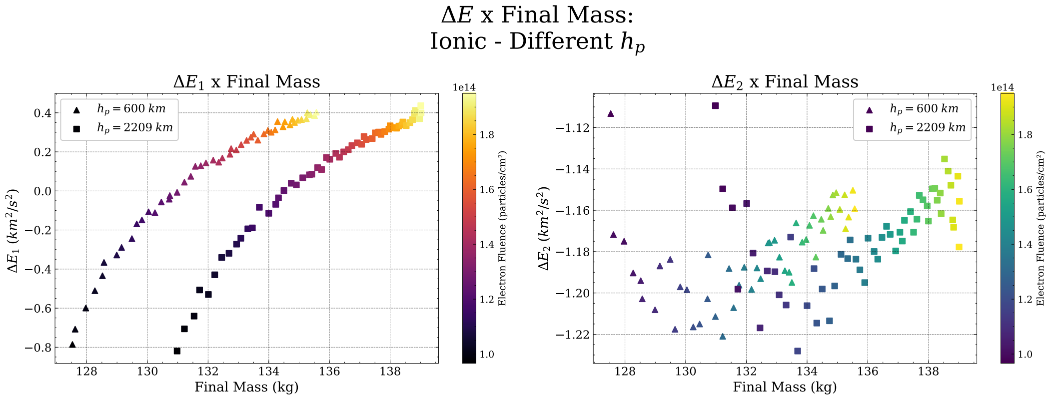

(a)

Figure 28. *Cont.*

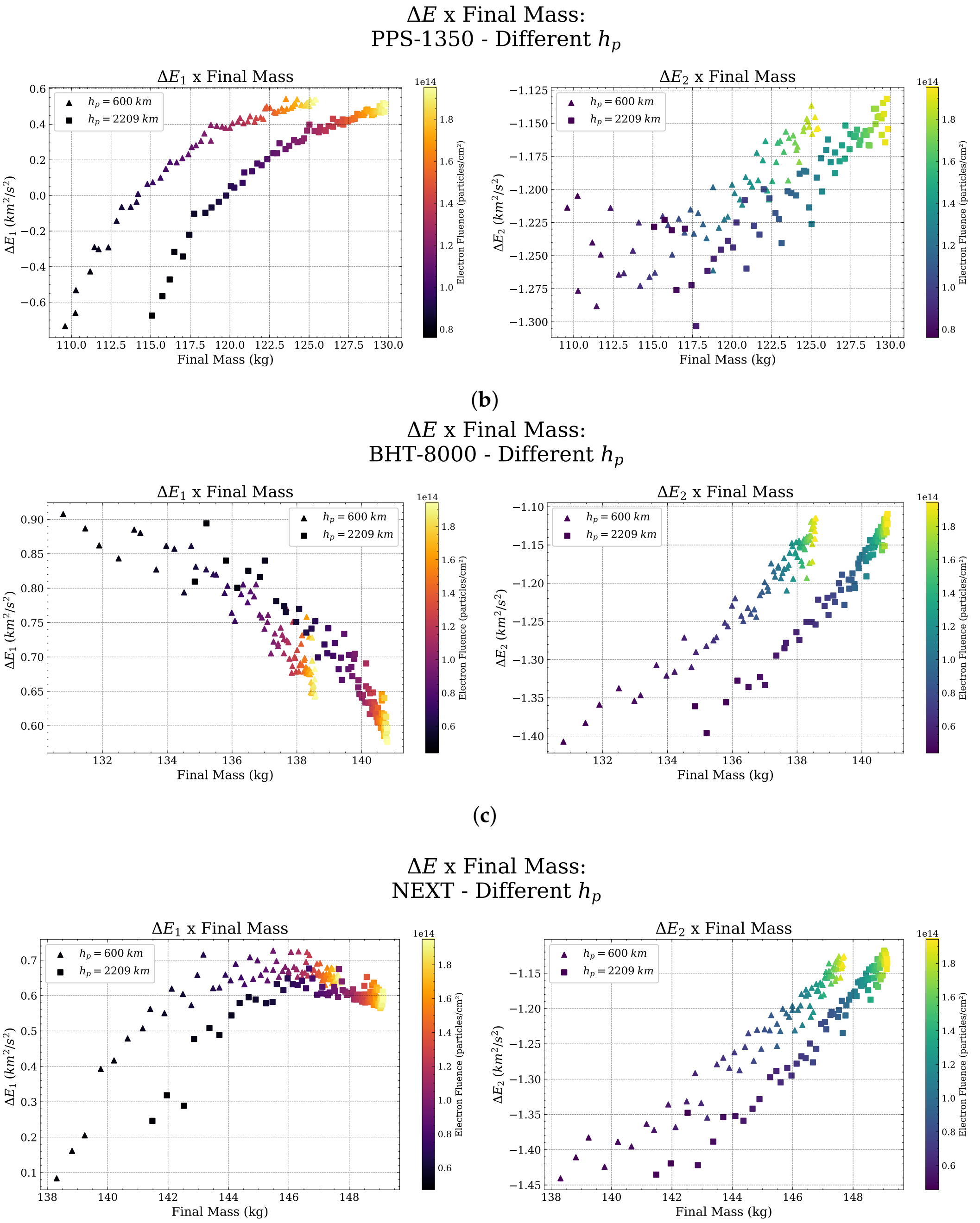

(**b**)

(**c**)

(**d**)

Figure 28. Energy gain, in its two configurations, as a function of the final mass, where the color of the dots represents the fluence of electrons, for the two initial perigee heights chosen (h_p = 600 km and h_p = 2209 km), with $e = 0$, $i_{moon} = 18°$ and $R_p = 1910.7$ km. (**a**) Ionic propulsion system. (**b**) PPS-1350 propulsion system. (**c**) BHT-8000 propulsion system. (**d**) NEXT propulsion system.

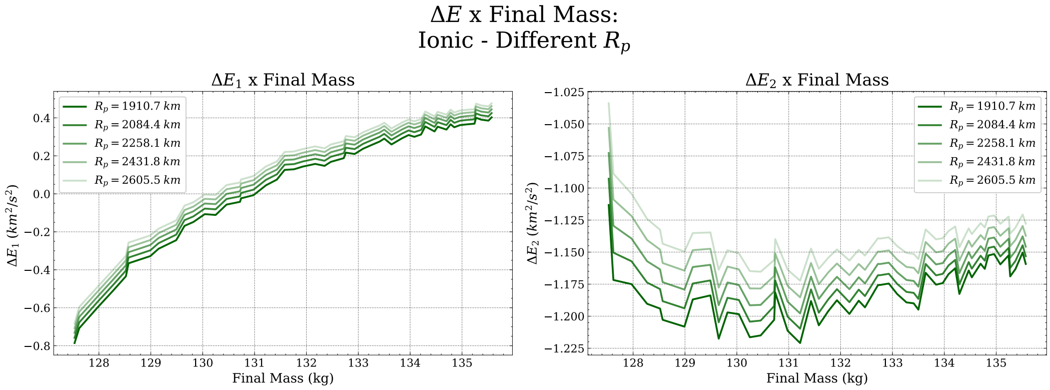

Figure 29. Energy gain, in its two configurations, as a function of the final mass for the five approximation distances R_p chosen initials (1910.7; 2084.4; 2258.1; 2431.8; 2605.5 km) and considering the ionic propulsion system, $h_p = 600$ km, $e = 0$ km, $i_{moon} = 18°$.

3.6. $\Delta V \times$ *Mass*

The graph in Figure 30 shows the increase in velocity ΔV as a function of the final mass, where the size of the dots represents the value of the electron flux absorbed by the spacecraft, for the four chosen propulsion systems—ionic, NEXT, BHT-8000 and PPS-1500—and considering the initial parameters as: $h_p = 600$ km, $e = 0$, $i_{moon} = 18°$ and $R_p = 1910.7$ km. Figure 31a–d show the same ΔV vs. final mass plots for each propulsion system separately, varying the parameter of initial eccentricity. Figure 32a–d show analogous plots, but this time varying the height of the perigee. Figure 33, finally, shows ΔV vs. final mass plots, varying the approximation distance.

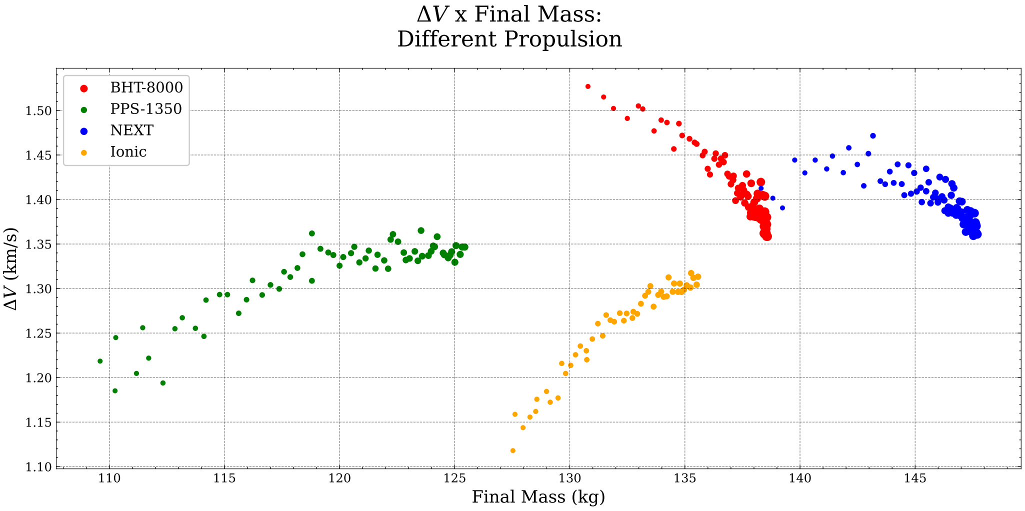

Figure 30. Velocity gain as a function of final mass, where the size of the dots represents the fluence of electrons, for the four chosen propulsion systems—ionic, NEXT, BHT-8000 and PPS-1500—and considering the initial parameters as: $h_p = 600$ km, $e = 0$, $i_{moon} = 18°$ and $R_p = 1910.7$ km.

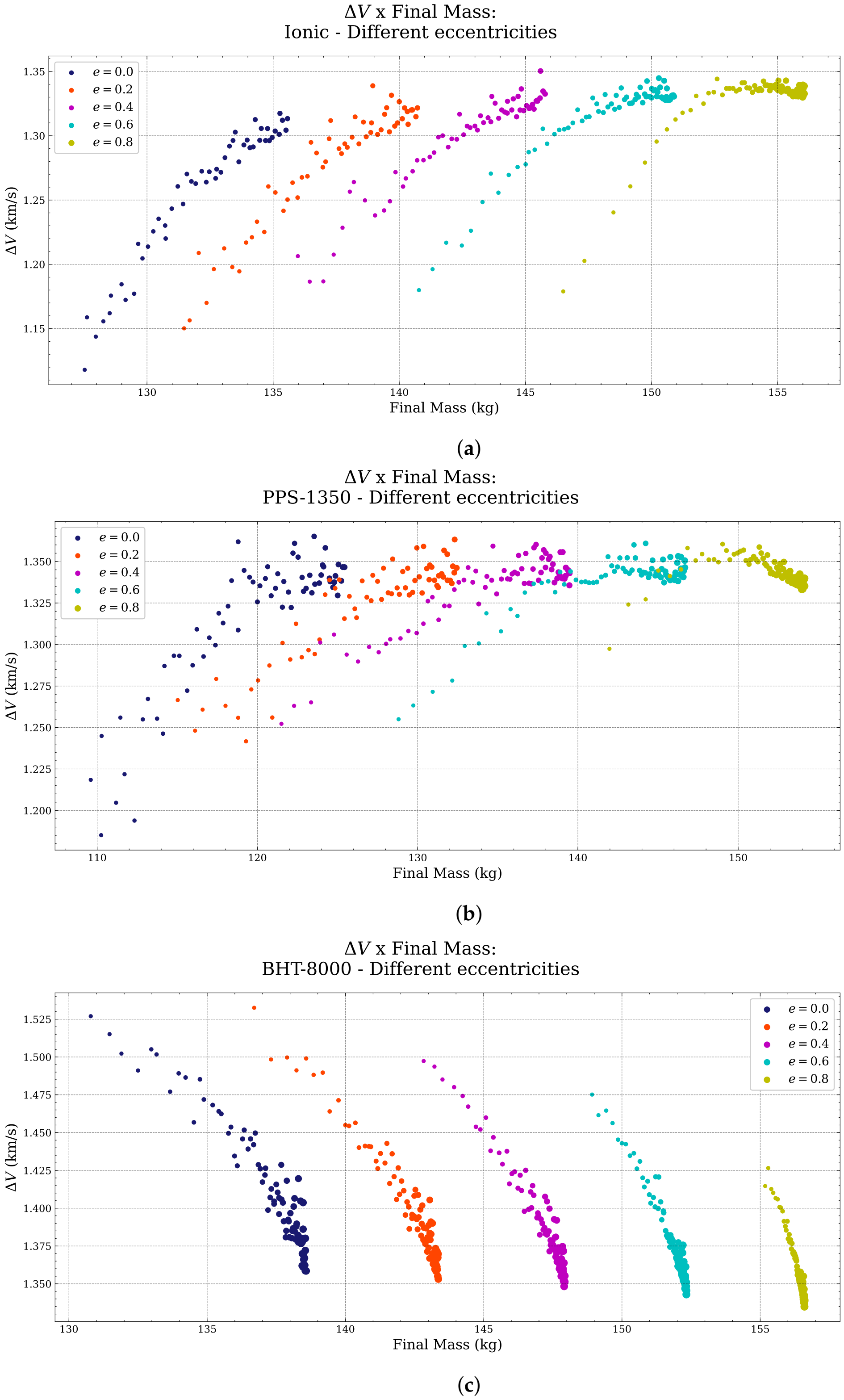

(**a**)

(**b**)

(**c**)

Figure 31. *Cont.*

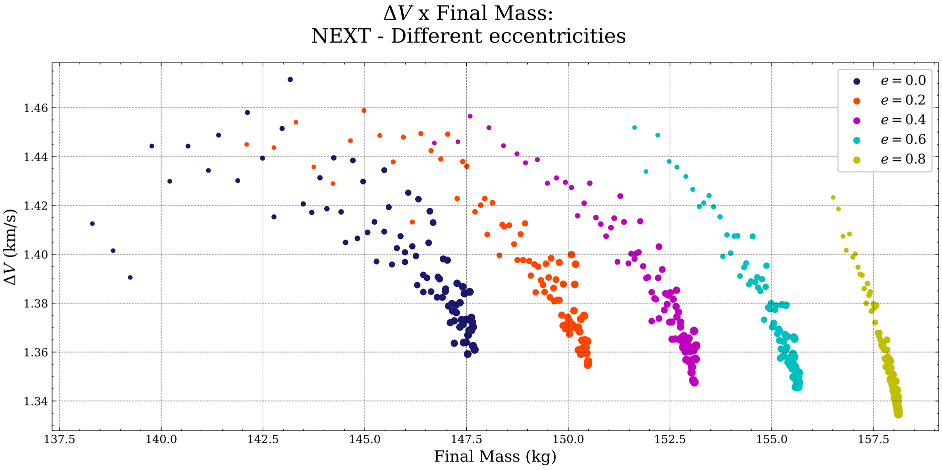
ΔV x Final Mass:
NEXT - Different eccentricities

(**d**)

Figure 31. Gain in velocity as a function of final mass, where the size of the dots represents the fluence of electrons, for the five initial eccentricities chosen (0; 0.2; 0.4; 0.6; 0.75), $h_p = 600$ km, $i_{moon} = 18°$ and $R_p = 1910.7$ km. (**a**) Ionic propulsion system. (**b**) PPS-1350 propulsion system. (**c**) BHT-8000 propulsion system. (**d**) NEXT propulsion system.

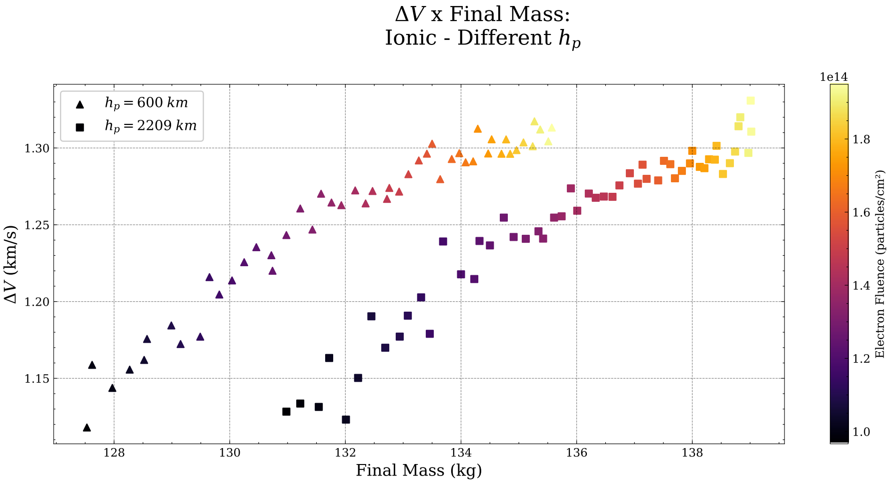
ΔV x Final Mass:
Ionic - Different h_p

(**a**)

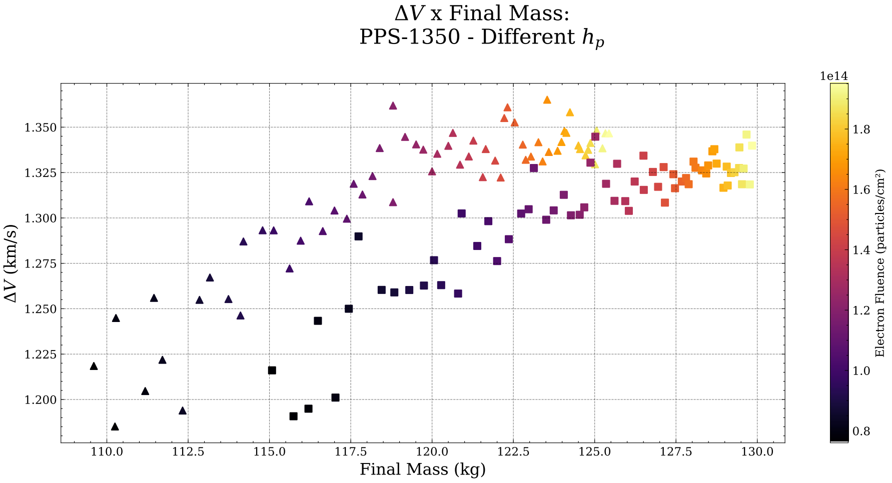
ΔV x Final Mass:
PPS-1350 - Different h_p

(**b**)

Figure 32. *Cont.*

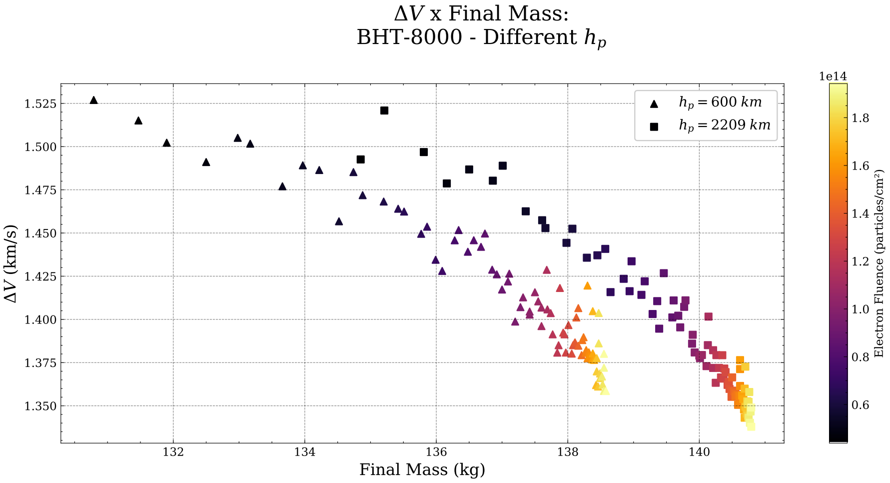

(**c**)

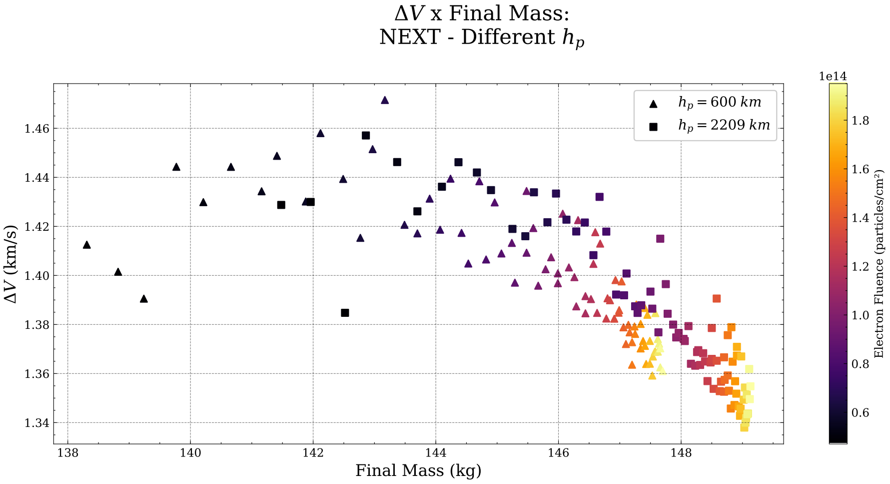

(**d**)

Figure 32. Gain in velocity as a function of the final mass, where the color of the dots represents the fluence of electrons, for the two initial perigee heights chosen ($h_p = 600$ km and $h_p = 2209$ km), with $e = 0$, $i_{moon} = 18°$ and $R_p = 1910.7$ km. (**a**) Ionic propulsion system. (**b**) PPS-1350 propulsion system. (**c**) BHT-8000 propulsion system. (**d**) NEXT propulsion system.

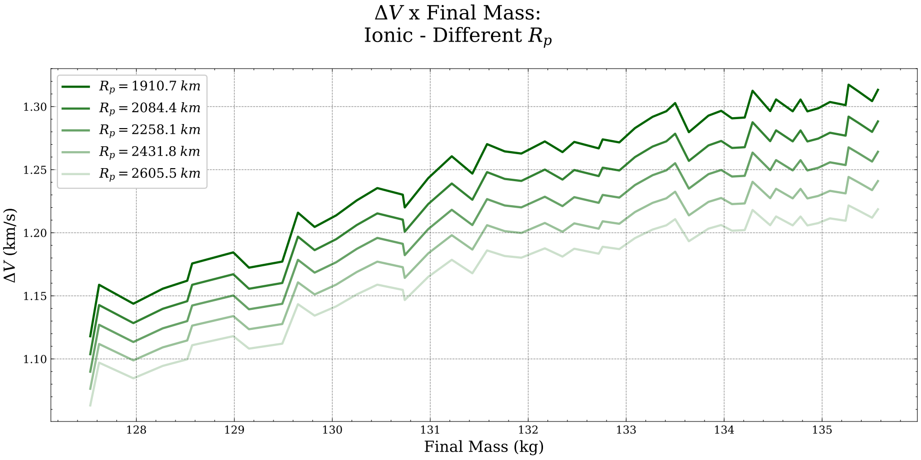

Figure 33. Speed gain as a function of final mass for the five initial chosen approximation distances R_p (1910.7; 2084.4; 2258.1; 2431.8; 2605.5 km) and considering the ionic propulsion system, $h_p = 600$ km, $e = 0$ km, $i_{moon} = 18°$.

3.7. Regression Models

After each of these improvements, graphical comparisons between the linear regression model and the artificial neural network were made, as shown in Figures 34 and 35, which should justify the decision of a robust machine learning algorithm. These plots change in inclination and use the following initial parameters as fixed inputs: $e = 0$, $h_p = 600$ km, $T = 72$ mN, $I_{sp} = 2700$ s.

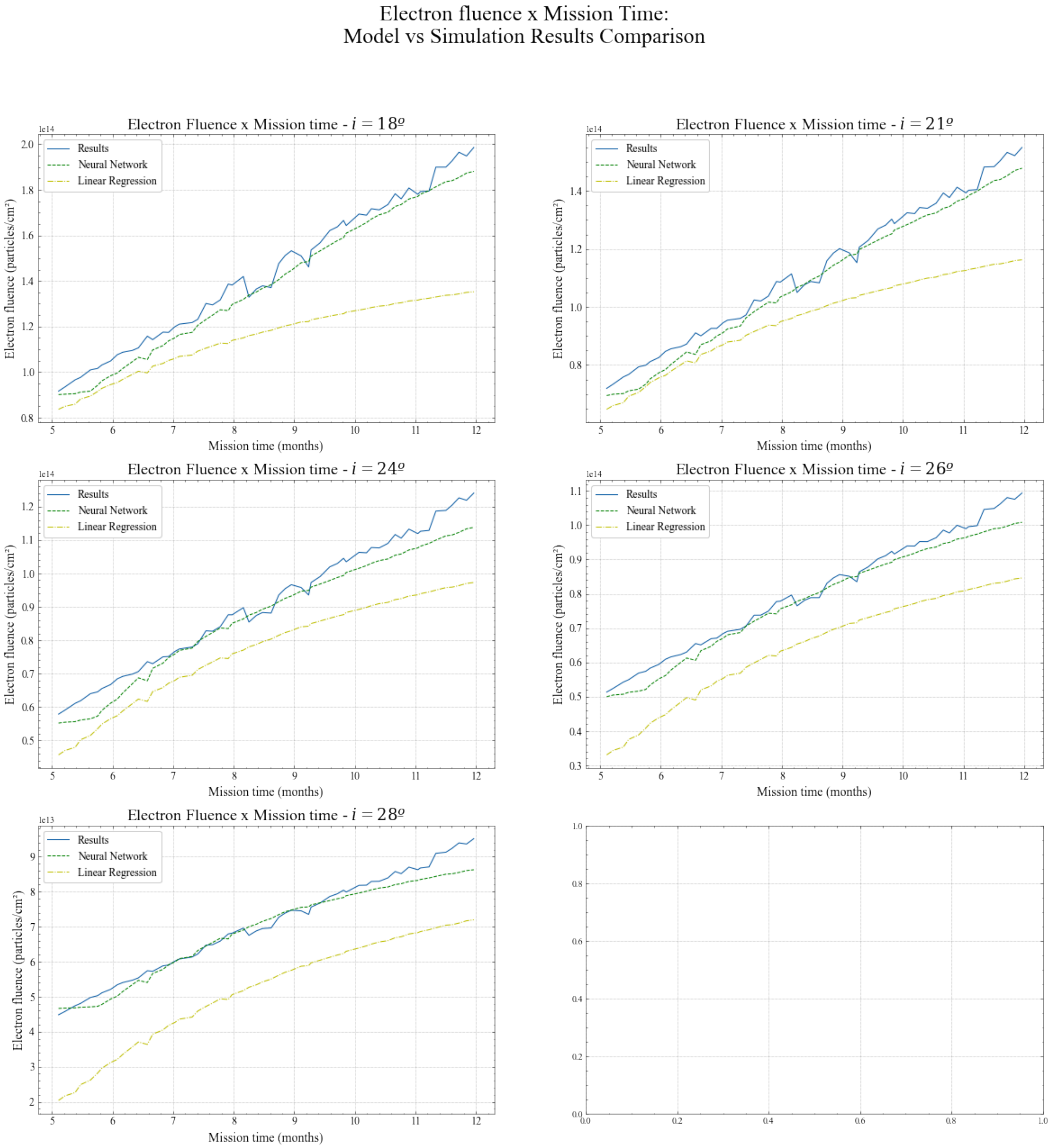

Figure 34. Model and data comparison for the electron fluences.

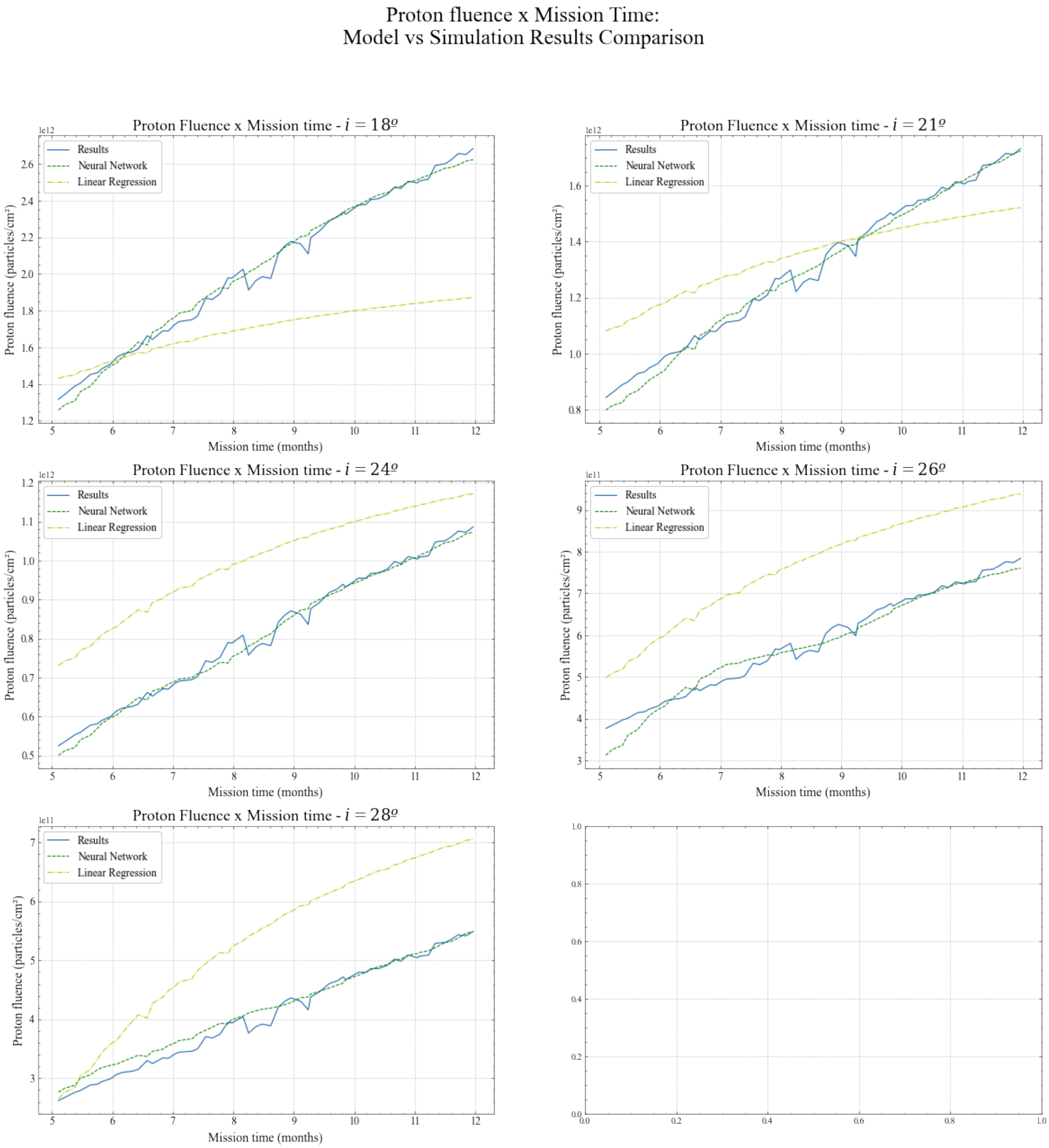

Figure 35. Model and data comparison for the proton fluences.

4. Discussion

4.1. Radiation vs. Time

In Figures 11–14, a linear trend for the fluences of protons and electrons with respect to the mission time can be observed.

From Figure 11, it can also be noted that the eccentricity of the initial orbit only affects the fluence of protons. This can be physically explained by the escape of the inner Van Allen belt (protons) during transfer when the initial orbit eccentricity is high; in the case of the outer belt (electrons), this escape does not happen, so its fluence is not affected by the initial eccentricity.

The graphs in Figure 12 show that the proton fluence is minimized with the use of the NEXT and BHT-8000 propulsion systems, which can be explained by their higher thrusts ($T = 236$ mN and $T = 449$ mN, respectively), since they allow an escape from the inner belt more quickly. In the case of the outer belt, the change of propulsion system does not practically affect the electron fluence.

Figure 13 shows that both proton fluence and electron fluence are affected by the inclination parameter, which is due to the fact that the greater the lunar inclination, the more it is at the edge of the Van Allen belts, be it the inner part (protons) or external (electrons). As demonstrated in the physical models presented in Figure 6, the particle fluxes at the upper and lower extremities are much lower, so it is expected that the increase in inclination minimizes the absorbed particle fluence during the trajectory.

Finally, in Figure 14 we can see once again that only in the case of proton fluence is there a considerable difference with the change in perigee height, which can be explained by the same reason as that affecting the initial eccentricity and propulsion system parameters: the eventual escape of the spacecraft is only allowed in the inner belt.

4.2. Final Mass × Time

Figures 15–17 show that the trend of increasing final mass with mission extension is not linear, but is quite predictable: more propellant consumption is needed for maneuvers that allow a shorter mission time.

Figure 15 presents another important aspect: the dependence of the parameter of mass on the initial eccentricity: the greater the eccentricity, the more mass is saved. This happens because the thrust arcs are at the perigee and therefore their effect is mainly to increase the apogee. So, if the initial orbit is already quite eccentric, the apogee is already higher, which reduces the fuel consumption necessary to achieve this purpose.

In Figure 16, the thrusters NEXT and BHT-8000 again stand out, corresponding to the highest final masses for the same initial orbital parameters. However, unlike the proton fluence versus time graph in Figure 12, the NEXT propellant is the one with the best performance for the final mass, which can be explained by its much higher specific impulse than the others, in addition to its high thrust.

From Figure 17, it is evident that the final mass has a direct dependence on the initial perigee height: the higher the perigee height, the more mass is saved. Similar to the case of Figure 15, the fuel consumption is minimized as the perigee is higher because, in this way, the initial orbit has an advantage regarding its final objective: reaching the lunar orbit. As the height of the perigee is greater, the apogee will also be greater, so there is less fuel consumption required to reach the final apogee that will have the moon as its destination.

4.3. $\Delta E \times$ Time

It can be noted in Figures 18–21 that there is an increasing trend in both the energy gain (ΔE_1) and the energy loss (ΔE_2) with mission time, but there is no linear pattern, as evidenced for the fluences of radiation versus time.

Another relevant aspect is highlighted in Figure 18, once again, by the NEXT and BHT-8000 propulsion systems, this time for the energy gain ΔE_1, given their thrust and specific impulse properties.

Based on the graphs in Figure 19a,b, it can be verified that, for the ionic and PPS-1350 systems, the increase in eccentricity has a positive effect on the energy gain, maximizing it; however, energy loss is reduced, which is an undesired effect if the mission's intent is to pass in front of the Moon to reduce energy. In the case of the NEXT propulsion system (Figure 19c), it is verified that the energy gain does not strongly depend on the initial orbit eccentricity, whereas the energy reduction is again minimized in magnitude as the eccentricity increases. For the BHT-8000 propulsion system (Figure 19d), it is clear that the trend is contrary to the others in terms of the energy gain. An increase in the initial eccentricity corresponds to smaller energy gains. For the energy loss ΔE_2, the larger eccentricity means smaller reductions, in modulus, in this parameter.

Based on Figure 20 (and the similar results obtained but not shown for the other propulsion systems), it is not possible to reach conclusions about the effect of perigee height on energy gains and losses with a swing-by. It is likely that there is not a strong dependency on this parameter with respect to ΔE.

In Figure 21, a clear trend can be seen: greater approximation distances to the moon imply a larger ΔE. This is valid for both energy gain ΔE_1 and energy loss ΔE_2. Therefore, there is a benefit in keeping away from the moon at the closest point of a swing-by, if an increase in energy is desired, whereas it is more interesting to move closer to it in the case of a reduction in energy, as this parameter will be minimized.

4.4. $\Delta V \times$ *Time*

In Figures 22–25, we can see that the dependence of velocity gain (ΔV) on mission time varies a lot, depending on several of the parameters involved.

First, it can be seen in Figure 22 that the tendency to increase speed depends strongly on the chosen propulsion system. Another relevant aspect is the highlighting, once again, of the NEXT and BHT-8000 propulsion systems, given their specific thrust and thrust properties.

For the variation in eccentricity in Figure 23a–d, it can be seen that the BHT-8000 and NEXT thrusters follow a similar tendency towards reducing the gain in velocity as the eccentricity of the initial orbit increases. The ionic and PPS-1350 systems, on the other hand, follow a contrary trend: the greater the eccentricity, the greater the ΔV, especially for short mission times. These results demonstrate how the dependence on the propulsion system is unpredictable, explaining the need to carry out case-by-case simulations according to the mission.

As in the case of ΔE, through Figure 24, it is not possible to reach conclusions about the effect of the height of the initial perigee on speed gain with the swing-by. It is likely that there is not a strong dependency on this parameter with respect to ΔV.

In Figure 25, one can see a clear trend: smaller approximation distances to the moon imply a larger ΔV. Therefore, there is a benefit in approaching closer to the moon at the closest point of a swing-by if you want to increase speed, whereas it is more interesting to keep it further away from it in cases where a reduction in speed is desired.

4.5. $\Delta E \times$ *Mass*

The plots from Figures 26–29 give us a lot of interesting information. First, we can again verify the results shown in Figures 15–17: the greater the final mass, the greater the absorbed radiation, since this parameter is also positively related to the mission time. Second, a clear trend is an increase in energy gain with increasing final mass (except for the BHT-8000 propulsion system), which is excellent for optimizing both parameters at the same time, at the cost of greater electron fluence.

Moving on to Figure 26, it can be verified, once again, that the propulsion systems NEXT and BHT-8000 are the highlights, maximizing both the final mass and the energy gain. Through this graph, it is possible to draw an overview of the swing-by, choosing values of ΔE, m and the propeller, besides having a qualitative idea of the radiation incident on the spacecraft.

Through Figure 27a–d, it is evident that an increase in eccentricity corresponds to greater final masses. In addition, the trend already shown in the graphs in Figure 26 can be seen: for energy gain, the ionic and PPS-1350 propulsion systems show an increase in ΔE_1 with the increase in mass, whereas BHT-8000 shows a reduction in ΔE with such an increase and NEXT shows both mentioned trends, the first for smaller masses and the second for larger final masses. As for the energy loss ΔE_2, the tendency of the four thrusters is to reduce the loss with the increase in the final mass.

From Figure 28a–d, it is possible to draw more conclusions about the effect of perigee height depending on the propulsion system. For the ionic and PPS-1350 systems, for example, Figure 28a,b make it clear that an increase in the initial h_p corresponds to a greater final mass, as we had already seen, but also at a smaller energy gain. For the ΔE_2 energy loss, however, no trend is clear for these two drive systems. For the systems NEXT and BHT-8000, in turn, it can be seen in Figure 28c,d that the increase in h_p corresponds to an increase in energy loss (module of ΔE_2), whereas nothing can be said about its effect on ΔE_1.

It is verified again, by Figure 29, that an increase in the distance of approximation to the moon increases the parameter ΔE, both for the configuration in ψ_1 and for ψ_2.

4.6. $\Delta V \times$ Mass

In addition to the information obtained with the graph of Figure 26—$\Delta E \times$ mass with different propulsion systems, we can obtain similar conclusions to those from Figure 30. First, we can again verify the results shown in Figures 15–17: the greater the final mass, the greater the absorbed radiation, since this parameter is also positively related to the mission time. Second, a clear trend is an increase in velocity gain with increasing final mass, which is excellent for optimizing both parameters at the same time, at the cost of greater electron fluence. Third, it is verified, once more, that the propulsion systems NEXT and BHT-8000 are the highest performing systems, maximizing both the final mass and the speed gain. Through this graph, it is possible to draw an overview of the swing-by, this time through the gains in speed, choosing values of ΔV, m and the propeller, in addition to obtaining a qualitative notion of the radiation incident on the spacecraft.

In Figure 31a–d, it is evident that an increase in eccentricity corresponds to higher final masses. In addition, the trend already shown in the graphs in Figure 30 can be seen: for the gain in energy, the ionic and PPS-1350 propulsion systems show an increase in the ΔV with the increase in mass, whereas BHT-8000 and NEXT show a reduction in ΔV with such an increase.

From Figure 32a–d, it is possible to draw more conclusions about the effect of perigee height depending on the propulsion system. For the ionic and PPS-1350 systems, for example, Figure 32a,b make it clear that an increase in the initial h_p corresponds to a greater final mass, as we had already seen, but also at a greater speed gain. For the BHT-8000 system, in turn, it is clear that the increase in h_p corresponds to an increase in the ΔV. As for the NEXT system, the curves are very similar to the BHT-8000, but the reduction in ΔV with the increase in h_p is not so explicit.

It is again verified, by Figure 33, that increases in the distance of approximation to the moon decrease the parameter ΔV.

4.7. Lunar Inclination and Regression Models

One can notice the influence of these new parameters in Figure 13, as the electron and proton fluences are clearly affected by the inclinations. Through the statistical model, it was also possible to verify the importance of this parameter's inclusion, since Tables 3 and 6 show that it had the lowest p-value, i.e., it was the most significant for the theoretical computation of the parameters of interest.

It is also clear from Tables 3 and 6 that three of the parameters are positively correlated to the fluence of particles: greater thrusts, mission times and final masses translate to a bigger fluence in protons and electrons. The other parameters, on the other hand, are all negatively correlated to the fluences of interest: a rise in either specific impulse, the initial orbit height of the perigee, eccentricity or lunar orbit inclination result in a lower amount of radiation absorbed in the trajectory. This preliminary analysis itself was proven valuable, which can be verified quantitatively by the high values obtained in the F- and t-tests and by the expressive values from R-squared and adjusted R-squared values, both for the protons and for the electrons.

Finally, the artificial neural network regression model yielded a greater accuracy when fitted to the data, which can be verified visually in Figures 34 and 35. Quantitatively, the ANN model resulted in much better statistical parameters of $R^2 = 0.997$ for the R-squared value and $MSE = 0.0002$ for the mean squared error, after several improvements such as feature scaling and hyperparameter optimization.

5. Conclusions

This paper provided an analysis of a myriad of factors involved in a low-thrust orbital transfer to the moon, considering the radiation exposure of the Van Allen belts. First, an overview of the optimization method used to find the best thrust arcs in a low-thrust transfer orbit was detailed. We then presented a full physical model for the Van Allen belts, starting out with a model of the Earth's magnetic field, followed by a discretization of the radiation belts in regions with fixed fluxes of particles, and finally a mathematical model for the dynamics of the Earth's magnetic axis. With these models, thousands of simulations provided quantitative results for the variables involved in the problem, such as final mass, mission time, radiation fluences, initial orbit eccentricity, the height of the perigee and the inclination of the moon's orbit. This great amount of data culminated in statistical analyses using regression and machine learning models, which were proven valid through several expressive statistical parameters. As a final step, a swing-by study was carried out to uncover hidden relationships between the gain in energy and velocity after an orbital maneuver with respect to other parameters of interest to a mission analyst, such as radiation exposure and final mass.

Author Contributions: Conceptualization, R.N.S., A.F.B.A.P. and V.M.G.; Methodology, R.N.S., A.S. and A.F.B.A.P.; Software, R.N.S. and A.S.; Validation, R.N.S. and V.M.G.; Formal analysis, R.N.S.; Investigation, R.N.S., A.F.B.A.P. and V.M.G.; Resources, A.F.B.A.P. and A.S.; Data curation, R.N.S. and A.S.; Writing—original draft preparation, R.N.S.; Writing—review and editing, R.N.S., A.F.B.A.P. and A.S.; Visualization, R.N.S.; Supervision, A.F.B.A.P.; Project administration, A.F.B.A.P.; Funding acquisition, A.F.B.A.P. All authors have read and agreed to the published version of the manuscript.

Funding: The authors would like to acknowledge their appreciation for the support from the National Council for Scientific and Technological Development (CNPq), through grant #432513/2018-3; for the support from Sao Paulo Research Foundation (FAPESP), through grants #2020/13557-7, #2018/16442-6 and #2016/24561-0; and the financial support from the Coordination for the Improvement of Higher Education Personnel (CAPES). This paper has been supported by the RUDN University Strategic Academic Leadership Program.

Institutional Review Board Statement: Not applicable.

Informed Consent Statement: Not applicable.

Data Availability Statement: Some or all data generated or used during the study are available in an online repository, which can be accessed in https://doi.org/10.5281/zenodo.5796896 (accessed on 28 February 2022) [26], in accordance with funder data retention policies. The repository holds both the simulation data from the Van Allen belts model and for the low-thrust transfer optimizer results. The latter includes calculations used in the swing-by analysis.

Conflicts of Interest: The authors declare no conflict of interest.

Abbreviations

The following abbreviations are used in this manuscript:

ANN	Artificial Neural Network
ANOVA	Analysis of Variance
CEV	Constant Exhaust Velocity
LEO	Low Earth Orbit
ML	Machine Learning
MSE	Mean Squared Error
NASA	National Aeronautics and Space Administration
NEXT	NASA's Evolutionary Xenon Thruster
ReLU	Rectified Linear Unit
SOI	Sphere of Influence
SVM	Support Vector Machine

Appendix A. Swing-By Maneuver

Figure A1 describes the swing-by technique and shows some of the variables involved. The variables are:

- R_p = periapse distance = maximum approach distance during the encounter (point P) between the ship and M2 (Moon);
- ψ = approach angle = angle between the periapse line - the line connecting M2 (Moon) to P - and the line between M1 (Earth) and M2 (moon);
- $\vec{V}_2$ = the speed of M2 (moon) in relation to M1 (Earth);
- $\vec{V}_\infty^-$, $\vec{V}_\infty^+$ = velocity vectors of the spacecraft relative to M2 (moon), before and after the encounter, respectively;
- $\vec{V}_p$ = velocity at point P;
- δ = half the curvature angle (the angle between $\vec{V}_\infty^+$ and $\vec{V}_\infty^-$);
- $\vec{V}_i$, $\vec{V}_o$ (not shown in the figure) = velocity vectors of the spacecraft relative to M1 (Earth), before and after the encounter, in an inertial frame, respectively.

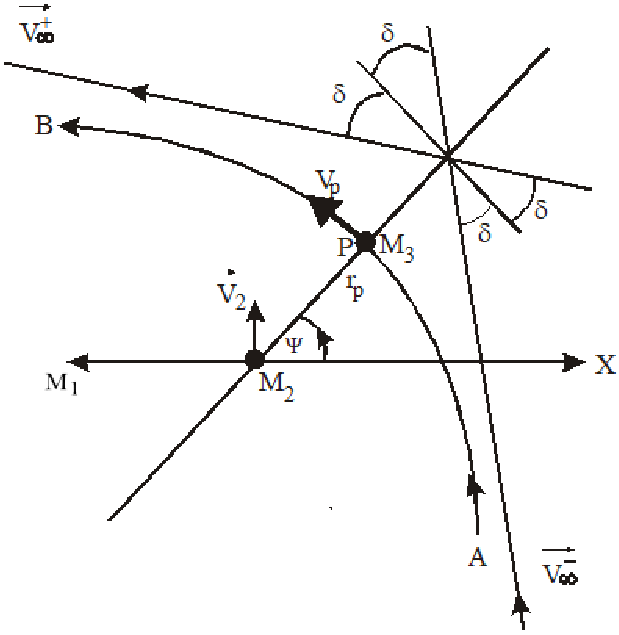

Figure A1. The swing-by maneuver and some of its variables.

To mathematically describe this problem, it is first necessary to use the theory of hyperbolic orbits, in order to obtain an expression for δ. This expression can be easily found in the literature and is given by [24]:

$$\sin\delta = \frac{1}{1 + \frac{R_p V_\infty^2}{\mu_{moon}}} \tag{A1}$$

where $\mu_{moon} = 4.90487 \times 10^{12}\ \mathrm{m}^3/\mathrm{s}^2$ is the gravitational parameter of the moon. Based on this equation and Figure A1, it is possible to identify that the independent variables that fully describe the swing-by maneuver are as follows:

1. V_∞, the magnitude of the spacecraft's velocity at infinity, before or after the next pass;
2. R_p, the distance from the periapse; and
3. ψ, the approach angle.

In the given context, the spacecraft has ended its low-thrust spiral trajectory and is heading for the moon in an orbit that escapes Earth. The study consists, therefore, in extracting optimal trajectories for the lunar swing-by, calculating the energy and speed gains when passing by the moon. For this purpose, it is necessary to calculate the approximation angle ψ, as well as the magnitude V_∞ of the speed at infinity. Another way to obtain these two pieces of information is through the radial and tangential components of the velocity to infinity, V_r and V_n, respectively. This is the method used in this work. Finally, by changing the periapse distance R_p as a program input, it is possible to optimize the value of these two variables and therefore maximize the increase in speed and energy.

First, we obtain the modulus of the inertial velocity V_i of the spacecraft with respect to the Earth at the Earth–moon distance. To do this, one has to isolate the velocity in the vis-viva energy conservation equation given the Earth–moon distance d_{EM}, which yields:

$$V_i = \sqrt{\mu_{earth}(\frac{2}{d_{EM}} - \frac{1}{a})} \tag{A2}$$

where a is the semi-major axis of the spacecraft's orbit as it passes the moon and d_{EM} is the distance between the center of the inertial frame (Earth) and the point where the spacecraft meets when it intersects with the moon.

For the tangential velocity V_n, we have the following expression:

$$V_n = \frac{\sqrt{\mu_{earth} p}}{R_p} \tag{A3}$$

where p is the semi-latus rectum. Finally, we calculate the radial velocity V_r as the complement of the tangential velocity V_n in the composition of the velocity vector V_i:

$$V_r = \sqrt{V_i^2 - V_n^2} \tag{A4}$$

The velocity at infinity is finally calculated as the modulus of the vector subtraction between the moon's velocity $\vec{V}_2$ and the spacecraft's inertial velocity with respect to Earth $\vec{V}_i$, as illustrated in Figure A2. Thus, we have the following relationship:

$$V_\infty = \sqrt{(V_n - V_2)^2 + V_r^2} \tag{A5}$$

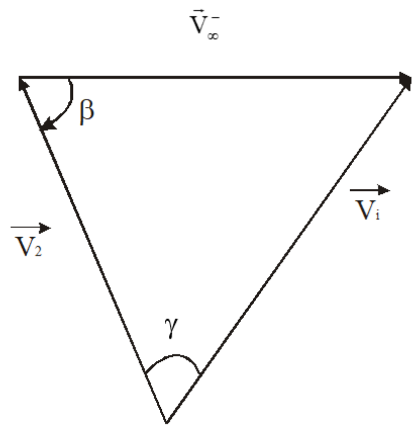

Figure A2. Vector sum involved in swing-by.

Through Figure A2, it is also possible to obtain the angle between the inertial velocity $\vec{V}_i$ of the space vehicle and the velocity of the Moon $\vec{V}_2$, called here β. It can then be obtained by the law of cosines, giving us:

$$\beta = \pm \arccos \frac{-(V_i^2 - V_2^2 - V_\infty^{-2})}{2 V_2 V_\infty^-} \tag{A6}$$

With this information at our disposal, the first important quantity to be calculated is the velocity variation ΔV, which represents the difference between the inertial velocities before and after the swing-by. Using simple vector algebra, it is possible to demonstrate the following equation [24]:

$$\Delta V = 2V_\infty \sin\delta \tag{A7}$$

Next, we need to calculate the change in energy ΔE, which will be done by calculating the approximation angle ψ. The two possible values for ψ are obtained from the geometry between the angles β and δ, and can be expressed mathematically as:

$$\psi = 180^\circ + \beta + \delta \tag{A8}$$

$$\psi = 360^\circ + \beta - \delta \tag{A9}$$

With the approach angle ψ in its two configurations, it is possible to calculate the respective energy variation ΔE. The following expression will be used without proofs, which can be found in [24]:

$$\Delta E = -2V_2 V_\infty \sin\delta \sin\psi \tag{A10}$$

References

1. Topputo, F.; Zhang, C. Survey of direct transcription for low-thrust space trajectory optimization with applications. In *Abstract and Applied Analysis*; Hindawi: New York, NY, USA, 2014; Volume 2014.
2. Pontryagin, L.S. *The Mathematical Theory of Optimal Processes*; John Wiley & Sons Inc.: Hoboken, NJ, USA, 1962.
3. Sukhanov, A.A.; Prado, A.F.B.A. Optimization of transfers under constraints on the thrust direction: I. *Cosm. Res.* 2007, *45*, 417–423. [CrossRef]
4. Sukhanov, A.A.; Prado, A.F.B.A. Optimization of transfers under constraints on the thrust direction: II. *Cosm. Res.* **2008**, *46*, 49–59. [CrossRef]
5. Sukhanov, A.A.; Prado, A.F.B.A. Inter-orbital low-thrust transfers in an arbitrary field of forces. *Cosm. Res.* **2013**, *51*, 147–163. [CrossRef]
6. Olson, W.P.; Pfitzer, K.A. A Quantitative Model of the Magnetospheric Magnetic Field. *J. Geophys. Res.* **1974**, *79*, 3739–3748. [CrossRef]
7. Garrett, H.B. *Guide To Modeling Earth's Trapped Radiation Environment*; American Institute of Aeronautics & Astronautics: Reston, VA, USA, 1999.
8. Marc-Andre, C.M. *Strategies and Geant4 Simulations for Radiation Protection on an EML-2 Mission*; ResearchGate: Berlin, Germany, 2015. [CrossRef]
9. SPENVIS. Background: Trapped Particle Radiation Models. 2010. Available online: https://www.spenvis.oma.be/help/background/traprad/traprad.html (accessed on 28 February 2022).
10. Gussenhoven, M.S.; Mullen, E.G.; Sagalyn, R.C. *CRRES/SPACERAD (Combined Release and Radiation Effects Satellite/Space Radiation Effects Program) Experiment Descriptions*; Air Force Geophysics Lab: Hanscom, MA, USA, 1985.
11. Sukhanov, A.; Barbosa, G.; Prado, A.; Winter, O.; Martins, J.; Macau, E. Estimation of the radiation hazard to a spacecraft passing the Van Allen belts in a low thrust transfer. In Proceedings of the IAA Conference on Dynamics and Control of Space Systems, 3 (DYCOSS) 2017, Rome, Italy, 28–31 January 2020.
12. Schmitt, R.N.; Barbosa, G.; Sukhanov, A.F.B.A.; Prado, A. Optimization of low thrust transfer orbits of a spacecraft considering the radiation hazard from the van allen belts. In Proceedings of the 2019 AAS/AIAA Astrodynamics Specialist Conference, AAS 19-802, Portland, ME, USA, 11–15 August 2019; Volume 171 of the Advances in the Astronautical Sciences Series.
13. Roncoli, R.B. *Lunar Constants and Models Document, JPL D-32296*; Jet Propulsion Laboratory, California Institute of Technology: Pasadena, CA, USA, 2005.
14. Observatory, U.N.; Office, H.N.A. *The Astronomical Almanac for the Year 1990*; US Government Printing Office: Chicago, IL, USA, 1990.
15. Felsentreger, T.L. *A Lunar Ephemeris, with the Earth's Equatorial Plane as Reference*; Technical Report; NASA Goddard Space Flight Center: Greenbelt, MD, USA, 1966.
16. Smola, A.J.; Schölkopf, B. A tutorial on support vector regression. *Stat. Comput.* **2004**, *14*, 199–222. [CrossRef]
17. Peng, H.; Bai, X. Comparative evaluation of three machine learning algorithms on improving orbit prediction accuracy. *Astrodynamics* **2019**, *3*, 325–343. [CrossRef]
18. Rubinsztejn, A.; Sood, R.; Laipert, F.E. Neural network optimal control in astrodynamics: Application to the missed thrust problem. *Acta Astronaut.* **2020**, *176*, 192–203. [CrossRef]
19. Pedregosa, F.; Varoquaux, G.; Gramfort, A.; Michel, V.; Thirion, B.; Grisel, O.; Blondel, M.; Prettenhofer, P.; Weiss, R.; Dubourg, V.; et al. Scikit-learn: Machine Learning in Python. *J. Mach. Learn. Res.* **2011**, *12*, 2825–2830.

20. Duchesnay, E.; Varoquaux, G.; Fritsch, V.; Gramfort, A.; Buitinck, L. Scikit-Learn: Pipeline.py. 2020. Available online: https://github.com/scikit-learn/scikit-learn/blob/0fb307bf3/sklearn/pipeline.py#L32 (accessed on 28 February 2022).
21. Kohlhase, C.E.; Penzo, P.A. Voyager mission description. *Space Sci. Rev.* **1977**, *21*, 77–101. [CrossRef]
22. Nock, K.T.; Upholf, C.W. Satellite aided orbit capture. In Proceedings of the AAS/AIAA, Provincetown, MA, USA, 25–27 June 1979; pp. 79–165.
23. Farquhar, R.; Muhonen, D.C.L.C. Trajectories and orbital maneuvers for the ISEE-3/ICE comet mission. *J. Astronaut. Sci.* **1985**, *33*, 235–254.
24. Broucke, R.A. The celestial mechanics of gravity assist. In Proceedings of the AIAA/AAS Astrodynamics Conference, Minneapolis, MN, USA, 15–17 August 1988.
25. Prado, A.F.B.A. Optimal Transfer and Swing-By Orbits in the Two- and Three-Body Problems. INPE-5572-TAE/022. Ph.D. Thesis, Department of Aerospace Engineering and Engineering Mechanics, University of Texas, Austin, TX, USA, 1993.
26. Schmitt, R.N. Van Allen Belts, SwingBy and Low-Thrust Simulation Data. 2021. Available online: https://zenodo.org/record/5796896 (accessed on 28 February 2022).